AO Photo-Injector: Experiments with Gun A June 97 to December 97

J.-P. Carneiro, R. A. Carrigan, M. S. Champion, A. Cianchi, E. R. Colby,
P. L. Colestock, H. T. Edwards, J. D. Fuerst, W. H. Hartung, K. P. Koepke,
M. Kuchnir, J. K. Santucci, L. K. Spentzouris
Fermi National Accelerator Laboratory, Batavia, Illinois 60510 USA

M. J. Fitch, A. R. Fry, A. C. Melissinos, B. D. Taylor
University of Rochester, Rochester, New York

27 January 1999

Contents

List of Figures

List of Tables

INTRODUCTION

An RF photo-injector was installed at Fermilab between January and June 97. The photo-injector produced its first beam on 4 June 97. This report provides a brief description of the accelerator and a summary of the experiments carried out through December '97.

1/ LAYOUT OF THE PHOTO-INJECTOR

The main parameters of the photo-injector installed at Fermilab are given below. These parameters are obtained by simulation.

RF Gun Parameters [Ref 1, p 116]

- Number of cells : 1.625
- Operating mode : $TM_{010,\pi}$
- Frequency : 1300 MHz
- Structure quality factor : 23601
- Operating Field at the Cathode : $E_{cathode} = 35\,MV/m$
- Power dissipated at $E_{cathode} = 35\,MV/m$: 2.2 MW
- Duty cycle : 1%
- Type of cathode : Cs_2Te
- Type of cavity : Cu

Beam Parameters [Ref 1, p 181]

- Energy : 4.5 MeV
- Energy spread : 0.8%
- Bunch charge : 10 nC
- Peak Current : 435 A
- RMS Normalized Emittance (u=x,y) : $\varepsilon_u = 20\pi\ mm.mrad$

Laser Parameters [Ref 2]

- Fundamental wavelength : 1054 nm
- UV wavelength : 263 nm
- Micro-pulse repetition rate : 1 MHz
- Micro-pulse length : 10 ps (2-12 ps)
- Macro-pulse repetition rate : 1 Hz
- Macro-pulse duration : 800 μs
- Energy per pulse : 1-10 μJ
- Type of oscillator : Nd:YLF
- Type of amplifier : Nd:glass

Installation at Fermilab

The facilities at Fermilab had limits :
- a problem with the slab amplifier of the laser made it difficult to obtain a macro-pulse of 800 micro-pulses. We did all of the experiments with 30 micro-pulses or less (it is also possible to obtain 800 micro-pulses with a repetition rate of 0.1 Hz).
- the second micro-pulse of the macro-pulse was missing because of a limitation in the laser electronics.

A schematic layout of the photo-injector is shown on the next page (Figure 1.1). The beam line has 6 crosses for diagnostics. The diagnostics in each cross (up, down, left, right in the direction of the beam propagation) consist of :

cross 1 :
- vacuum diagnostics (ionization gauge and residual gas analyzer)
- pumping port
- viewport for camera to observe the cathode
- viewport for entrance of the laser

cross 2 :
- emittance probe (slits)
- Cr doped Al_2O_3 (ruby) screen (2"× 2")
- ion-getter pump
- viewport for CCD camera (SN 241022)

cross 3 :
- Optical Transition Radiation (OTR) screen
- Cr doped Al_2O_3 (ruby) (28 mm × 28 mm × 1mm)
- ionization gauge
- viewport for CCD camera (SN 252089) and Intensified camera.

cross 4 :
- empty
- empty
- ionization gauge
- empty

cross 5 :
- YAG screen (circular with 25 mm diameter)
- ion-getter pump
- empty
- viewport for CCD camera (SN 252087)

cross 6 :
- YAG screen (circular with 25 mm diameter)
- ion-getter pump
- viewport CCD camera (SN 241021)
- empty.

Others diagnostics have been installed in the beam line :

- 2 Integrating Current Transformers (ICTs) to measure the charge of the beam, one after the secondary solenoid and the other between crosses 2 and 3.
- 2 trim magnets to steer the beam, one after cross 1 and the other after cross 2.
- 2 quadrupoles located between crosses 2 and 3.
- 1 Beam Position Monitor (BPM) to measure the transverse position of the beam, located between cross 1 and 2.
- 2 Faraday Cups, one at the end of the beam line, the other at the end of the bend.

In the following sections we describe the experiments with the RF Gun. The first experiment we present is the spectrometer calibration because of its importance for measurement of the beam energy.
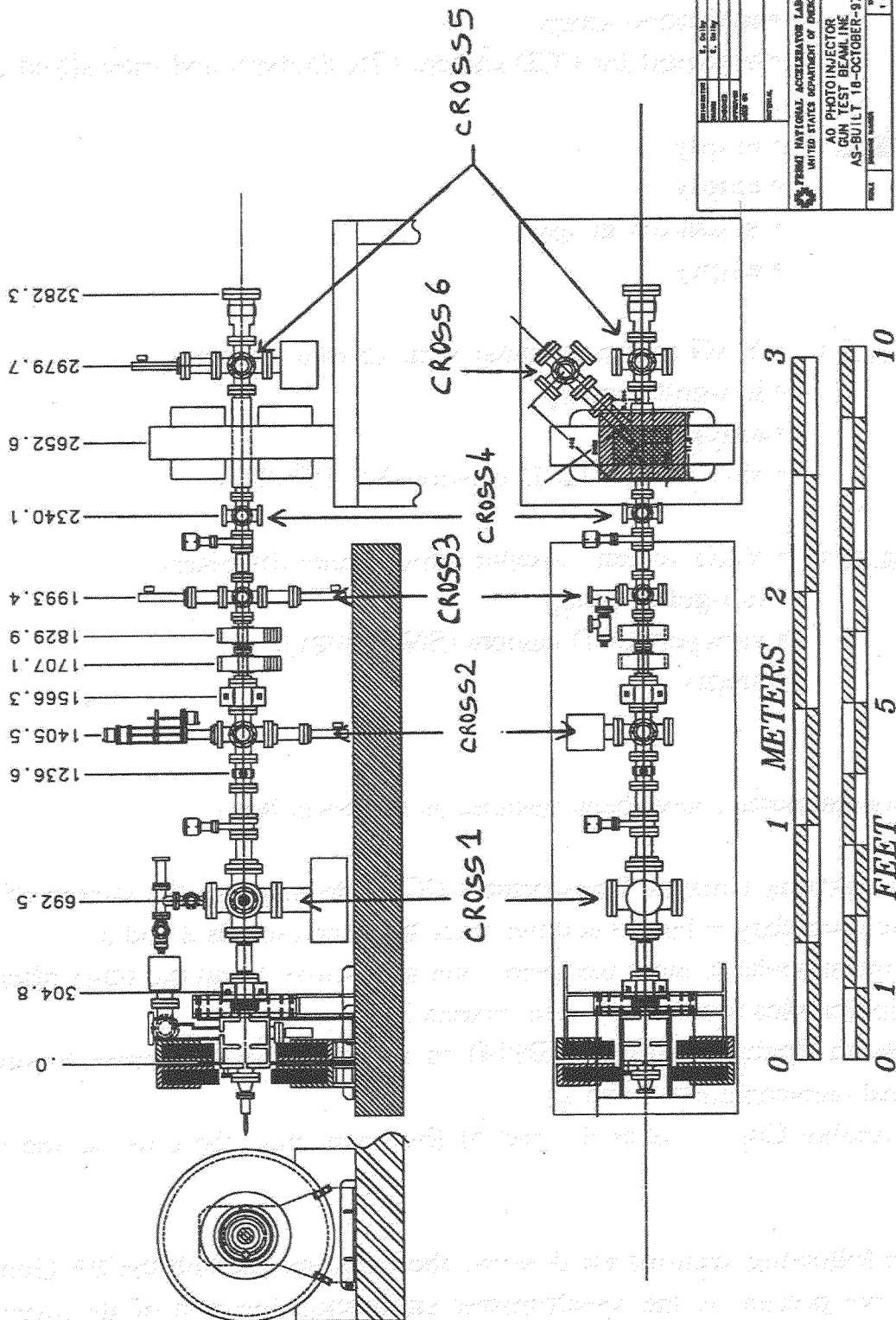
Figure 1.1. Schematic layout of the photo-injector

2/ SPECTROMETER CALIBRATION

The spectrometer used in the AO photoinjector is a dipole with an angle $\theta = 45°$, an iron length $L_I = 165$ mm and a gap length $L_G = 115$ mm. We define the magnetic length L_M of the dipole to be equal to the iron length plus half a gap in each side of the iron, so $L_M = 280$ mm. The magnetic length corresponds to the magnetic field experienced by the particles. We associate a bending radius to the magnetic field of $\rho = 40.2$ cm. This radius will be considered in the following as the bending radius of the dipole.

An application of Ampère's Law gives the relationship between the magnetic field produced by the dipole and the current in the windings :

$$\boxed{B[T] = \frac{\mu_0 NI}{L_G}}$$

with :
- μ_0 = the permeability of the free space = $4\pi.10^{-7}$ H/m
- N = Number of turns = $12 \times 29 \times 2$
- L_G = Length of the gap [m] = 11.5×10^{-2} m
- I = Current in the windings [A]

we get :
$$B[T] = 7.61 \times 10^{-3} I[A]$$

To check the validity of this theoretical relation, we put a Hall probe above the beam tube in the middle of the spectrometer and we measured the magnetic field as a function of the current set by the Macintosh.

We obtained 6 sets of data for several current ranges between -10 Amp and +10 Amp. Each set of data was fitted by a line and the mean of all the lines gave $B[T] = 7.18 \times 10^{-3} I[A]$. We made also an hysteresis measurement between -10 Amp and +10 Amp. We found a weak hysteresis effect in the dipole.

The above relation gives the magnetic field at a point above the beam tube, but we were interested in the magnetic field in the middle of the beam tube, where the beam is located. To measure the latter, we compared Hall probe readings above and in the

middle of the beam tube for the same dipole current. We saw that the magnetic field decreased from the top to the middle by a factor of 1.03. This indicates that, in the middle of the beam tube : $B[T] = 6.97 \times 10^{-3} I[A]$.

The experimental coefficient differs from the theoretical value by less than 10%. Consequently, throughout this report, we will use the relation :

$$B[T] = 7 \times 10^{-3} I[A] \tag{2.1}$$

We also measured the profile of the magnetic field in the middle of the spectrometer. This profile is plotted in Figure 2.1. The abscissa is distance in the direction of propagation of the beam. The abscissa zero is the middle of the iron length.

Profile of the magnetic field in the spectrometer in the direction of propagation of the beam
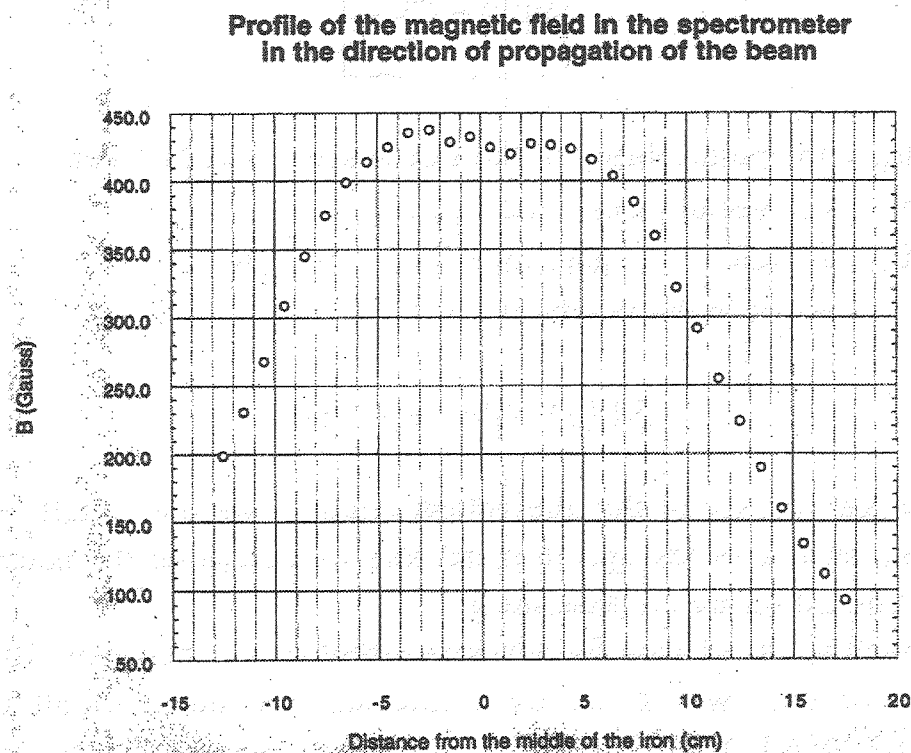
Figure 2.1. Profile of the magnetic field in the spectrometer

Energy measurement : principle   [Ref 3, p. 61]

We used the definition of the magnetic rigidity in the spectrometer magnet to obtain the beam energy :

$$P[GeV/c] = \frac{1}{3.3356} \times (B\rho)[T.m]$$

(3.1)

using $\rho=40.2$ cm and equation (1), we get :

$$P[MeV/c] = 0.84 \times I[A]$$

(3.2)

where I is the current required in the spectrometer to obtain a horizontally narrow image of the beam on the YAG screen located in cross 6.

Energy spread measurements : principle   [Ref 3, p. 91]

We used the dipole to measure the energy spread. A particle's path through the dipole depends on its momentum. If we consider that the phase advance is the same for all the particles, the horizontal spread can be written as the sum of 2 terms :

$$x_{max}(s) = \sqrt{\frac{\beta(s)\varepsilon_g}{\pi}} + D_x(s)\delta_{max}$$

with : • ε_g = geometrical emittance

• $\delta_{max} = \frac{\Delta P}{P_0}$ = energy spread of the beam.

• $D_x(s) = T_{13}$

For a dipole with angle θ, the T_{13} coefficient of the transport matrix to a screen located at a distance L downstream is:

$$T_{13} = [\rho(1-\cos\theta) + L\sin\theta]$$

We have :
- $\rho = 40.2$ cm
- $\theta = \pi/4$
- L = the distance between the end of the magnetic field and the screen = 26.1 cm

So that :

$$\boxed{D_x(s) = T_{13} = 0.302}$$

In order to obtain the energy spread δ_{max} from $x_{max}(s)$, we need to minimize the $\beta(s)$ function. To minimize this function, we need a horizontal focus in cross 6. We have two options :

- We can neglect the $\beta(s)$ function, in which case :

$$\delta_{max} = \frac{x_{max}}{T_{13}} = \frac{x_{max}}{0.302}$$

- We can simulate the beam envelope using Trace 3D and obtain a value of $\beta(s)$ and ε_g in cross 6. In this case :

$$\delta_{max} = \left[x_{max} - \sqrt{\frac{\beta(s)\varepsilon_g}{\pi}} \right] \times \frac{1}{0.302}$$

Experiment and results

We focused the beam horizontally on the YAG screen in cross 6 and we recorded 10 images of the beam spot. The intensity in the dipole to focus the beam was 5.6 A. The images are located in the folder Energy/energy spread_12/17/97 with the name cross5_energy_5.6A#00 to ##10. We present in Figure 3.1 the beam intensity profile from the image cross5_energy_5.6A#09. We fit the beam to a Gaussian distribution.

Equation (3.2) gives us a beam energy of :

$$\boxed{E = 4.73 \text{ MeV}}$$

8

From the Gaussian fit shown in Figure 3.1, we obtained the width σ_x of the beam : $\sigma_x = 17.787$ pixels. The calibration of the screen in cross 5 gives 1 pixel = 0.13 mm which gives $\sigma_x = 2.32$ mm.

- **Neglecting $\beta(s)$**

$$\delta = \frac{2.32 \times 10^{-3}}{0.302} = 7.68 \times 10^{-3}$$

- **Using Trace 3D**

A simulation of the beam envelope with Trace 3D gives in cross 6 $\beta(s) = 0.49$ mm / mrad and $\varepsilon_g = 1.05\,\pi\,\text{mm}\,\text{mrad}$, so that :

$$\delta = \left[2.32 - \sqrt{0.49 \times 1.05}\right] \times \frac{10^{-3}}{0.302} = 5.31 \times 10^{-3}$$

$y = m1+m2*exp(-((m3-M0)^2/(2...$		
	Value	Error
m1	102.16	14.897
m2	879.94	17.518
m3	52.514	0.31868
m4	17.787	0.51671
Chisq	4.1121e+05	NA
R	0.98072	NA
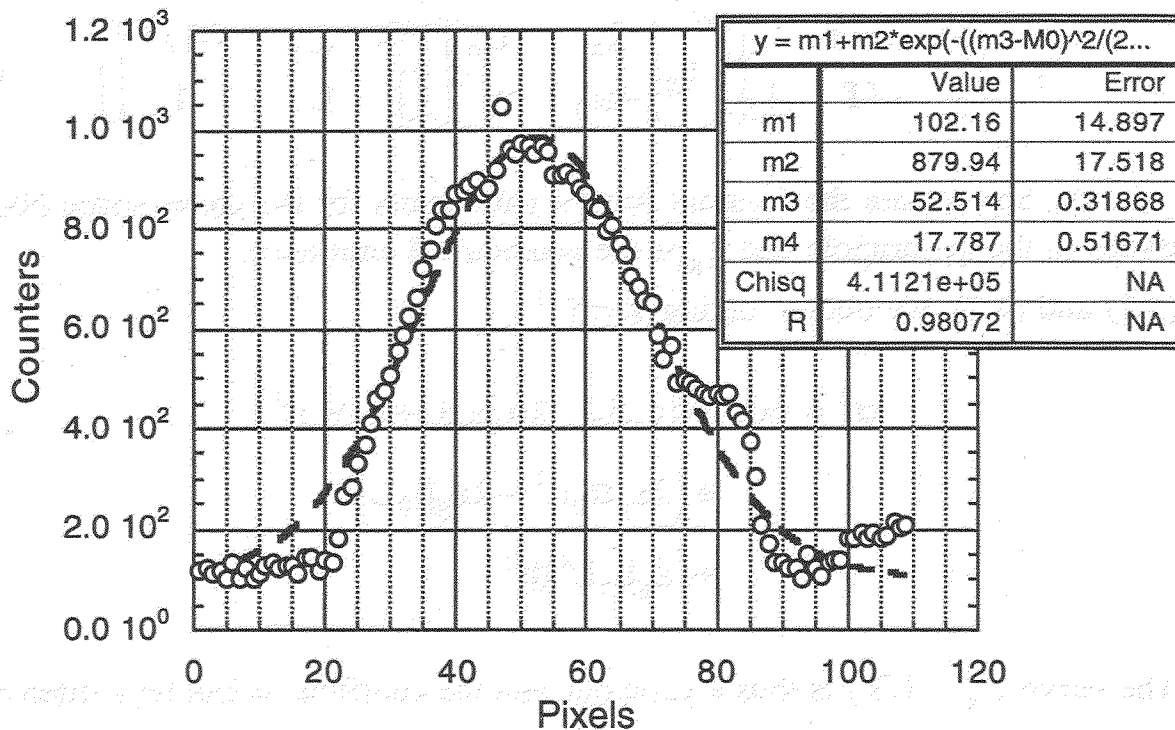
Figure 3.1. Profile of the beam in cross 6 (energy and energy spread)

4.1. Quadrupole Scan Measurement

Principle

We used a quadrupole to focus the beam horizontally and vertically on a screen located at a distance L=163 cm from the quadrupole.

If we consider the quadrupole as a thin lens of focal length f, the matrix of the beam at the screen (σ_f) can be related to the matrix of the beam at the entrance to the quadrupole (σ_o) by:

$$\sigma_f = T\sigma_o T^t = \begin{bmatrix} \langle xx \rangle & \langle xx' \rangle \\ \langle x'x \rangle & \langle x'x' \rangle \end{bmatrix} \tag{4.1}$$

T is the transport matrix between the quadrupole and the screen. Putting in T, we obtain:

$$\sigma_f = \left(\begin{bmatrix} 1-L/f & L \\ -1/f & 1 \end{bmatrix} \left(\varepsilon_g \begin{bmatrix} \beta_0 & -\alpha_0 \\ -\alpha_0 & \gamma_o \end{bmatrix} \right) \begin{bmatrix} 1-L/f & -1/f \\ L & 1 \end{bmatrix} \right) \tag{4.2}$$

where α_0, β_0, and γ_0 are the Courant Snyder parameters for the phase-space ellipse at the entrance to the quadrupole and ε_g is the geometrical emittance.

From (4.1) and (4.2), we obtain, taking $k = f^{-1}$

$$\sigma_x^2 = \langle xx \rangle = \left(\varepsilon_g \beta_0 - 2\alpha_0 \varepsilon_g L + \varepsilon_g \gamma_o L^2 \right)$$
$$+ \left(2\varepsilon_g \alpha_0 L^2 - 2\varepsilon_g \beta_0 L \right) k$$
$$+ \left(\varepsilon_g \beta_0 L^2 \right) k^2$$

The curve $\sigma_x^2 = f(k)$ is thus a parabola, and the coefficients can be written as:

$$a_0 = \varepsilon_g \beta_0 - 2\alpha_0 \varepsilon_g L + \varepsilon_g \gamma_o L^2$$

$$a_1 = 2\varepsilon_g \alpha_0 L^2 - 2\varepsilon_g \beta_0 L$$

$$a_2 = \varepsilon_g \beta_0 L^2$$

This parabola can be produced experimentally by observing the beam spot size on the screen while varying the strength of the quadrupole. The parameters α_0, β_0, and ε_g can be related to a_0, a_1, and a_2 :

$$\beta_0 = \frac{2a_2}{P}$$

$$\alpha_0 = \frac{2a_2 + La_1}{PL}$$

$$\varepsilon_g = \frac{P}{2L^2}$$

with:

$$P = \sqrt{4a_0 a_2 - a_1^2}$$

The above analysis doesn't take into account **space charge** forces or other perturbative effects such as geometric or chromatic aberration. In the AO photoinjector, the space charge alone makes this model inaccurate.

To include the space charge forces and the other effects, we used the program **Trace 3D.** We assumed that for fixed energy, charge, frequency, and drift length L, there is only one set of parameters (α_0, β_0, ε_g) that fits the curve $\sigma_x^2 = f(k)$.

Experiment

We used 10 pulses of charge 1.2 nC each. We measured the beam energy after the experiment with the spectrometer magnet using the method described in §2, and we found an energy of 4.52 MeV (spectrometer current = 5.321 A, image = Emittance/emittance with quadrupole scan/sp_10p_1.2nC_5.321A/).

We did a quadrupole scan using the second quadrupole, with the first quadrupole degaussed and turned off. We scanned the current in the second quadrupole from -4

Amp to +4 Amp and we recorded the images of the beam on the screen in cross 3, located 163 mm from the quadrupole. We obtained 4 images with vertical focussing (I=-4 Amp to -1 Amp) and 4 images with an horizontal focussing (I=1 Amp to 4 Amp). For I=0 we didn't obtain a particular focussing. These images are in the folder Emittance/ Emittance with quadrupole Scan/Quad_Scan 12/19/97.

To analyze these images, we assumed a Gaussian beam and determined the width σ_x for each image. To obtain $\sigma_x^2 = f(k)$ we converted the quadrupole current into the k coefficient using the following relations:

$$k = \frac{1}{f} \quad \left[m^{-1} \right]$$

with :

$$f = \frac{\gamma mc}{qL_Q} \times \frac{R_Q}{B} \quad [m]$$

where :
- f = the focal length of the quadrupole
- L_Q = length of the quadrupole [m]
- R_Q = radius of the quadrupole [m]
- B = magnetic field [T]. For this quadrupole a previous study

showed that:

$$B[G] = -1.003 + 92.54 \times I - 0.05407 \times (I^2) - 0.1321 \times (I^3)$$

with I being the intensity in Ampere set in the quadrupole :

In the present case :
- $E = \gamma mc^2 = 4.52$ MeV
- $L_Q = 7.6$ cm
- $R_Q = 1.8$ cm

The curves $\sigma_x^2 = f(k)$ and $\sigma_y^2 = f(k)$ are plotted in Figures 4.1 and 4.2. The fit of the curves by Trace 3D is given by the dotted line. We tried first to use the relation between the coefficients a_0, a_1, and a_2 of the parabola $\sigma_x^2 = f(k)$ we obtained experimentally and to find the coefficients α_{X0}, β_{X1}, ε_g via the model we described above (without space charge).

12

Results using the coefficients of the parabola (without space charge)

The fit of $\sigma_x^2 = f(k)$ of Figure 4.1 gives :

- $a_0 = 46.779 \quad mm^2$
- $a_1 = -10822 \quad mm^3$
- $a_2 = 6.3629 \times 10^5 \quad mm^4$

and using the relations above we obtain :

- $\alpha_{X0} = 262.41$
- $\beta_{X0} = 912.635 \; mm / mrad$
- $\varepsilon_{X,g,N} = 2.32 \times 10^{-1} \; \pi mm.mrad$

As expected, these results are not credible and we have to use **Trace 3D.**

Results using Trace 3D

The coefficients which fit the curve $\sigma_x^2 = f(k)$ are:

- $\alpha_{X0} = -19$
- $\beta_{X0} = 40 \; mm / mrad$
- $\varepsilon_{X,g,N} = 9.14 \; \pi mm.mrad$

where $\varepsilon_{X,g,N}$ is the normalized geometrical horizontal emittance.

The coefficients which fit the curve $\sigma_y^2 = f(k)$ are

- $\alpha_{Y0} = 3$
- $\beta_{Y0} = 40 \; mm / mrad$
- $\varepsilon_{Y,g,N} = 6.86 \; \pi mm.mrad$

where $\varepsilon_{Y,g,N}$ is the normalized geometrical vertical emittance.

Figure 4.1. Quadrupole Scan - Emittance (X-X')
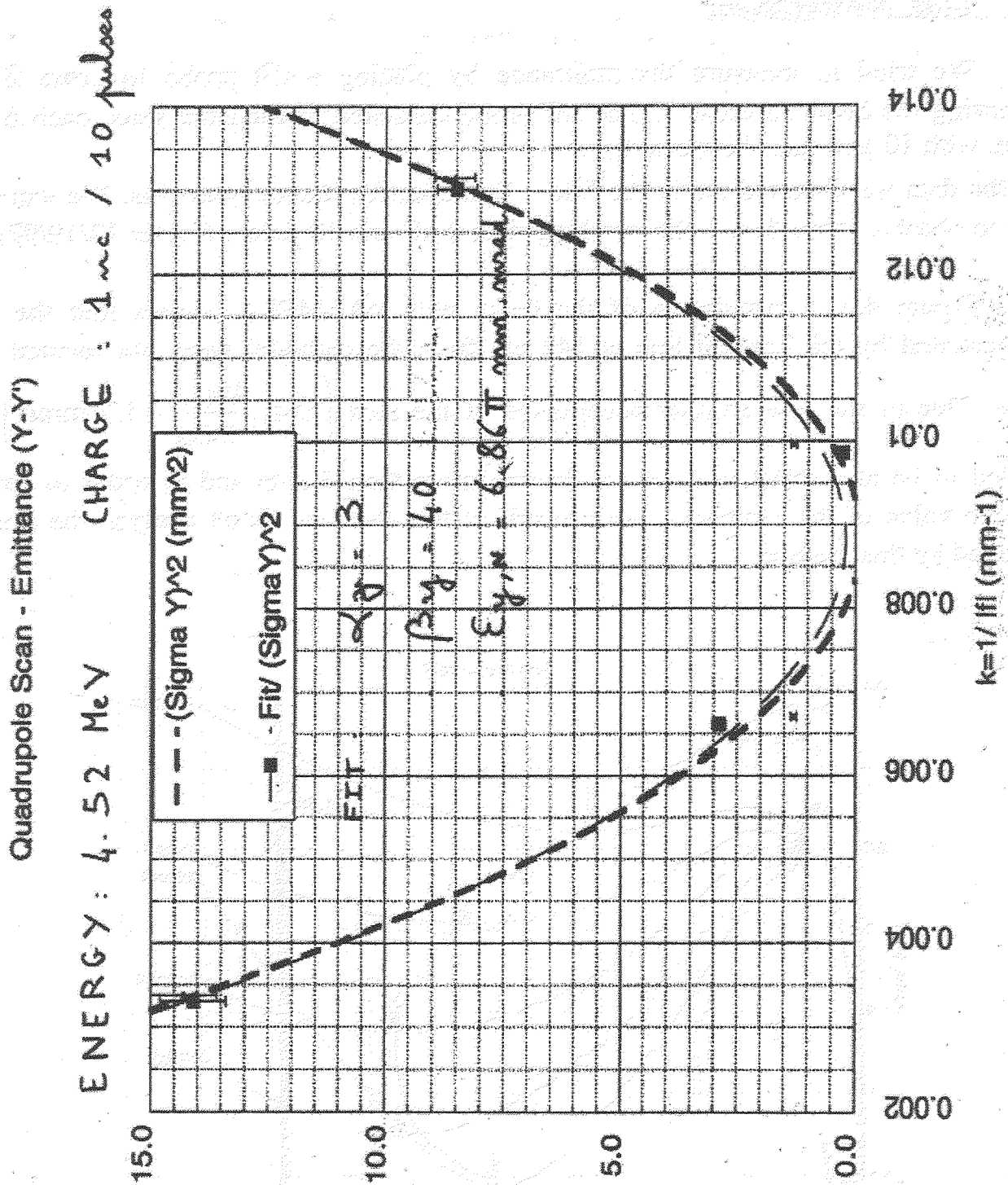
Figure 4.2. Quadrupole Scan - Emittance (Y-Y').

15

4.2. Slits Measurement

We tried to measure the emittance by placing a slit probe in cross 2 and observing the beam in cross 3. The slit probe consisted of tungsten slats, each 6 mm wide, with 10 μm gaps between them.

All the data we obtained are in the folder Emittance/emittance with slits. We were not able to observe more than 3 slits working with 2 nC and 10 pulses (folder 12/19/97).

Figure 4.3, a simulation of the beam with PARMELA, shows that the slits (represented by the vertical line at 142 cm from the cathode) were not located in a waist. Due to the low angular acceptance of the slits $\left(\theta \cong \dfrac{10\mu}{6000\mu} = 1.7 \text{ mrad} \right)$ we needed to be at a waist in order to observe more than 3 slits and in order to have a reliable value of the emittance. As a result of this fact, we didn't analyze the images obtained by this method.
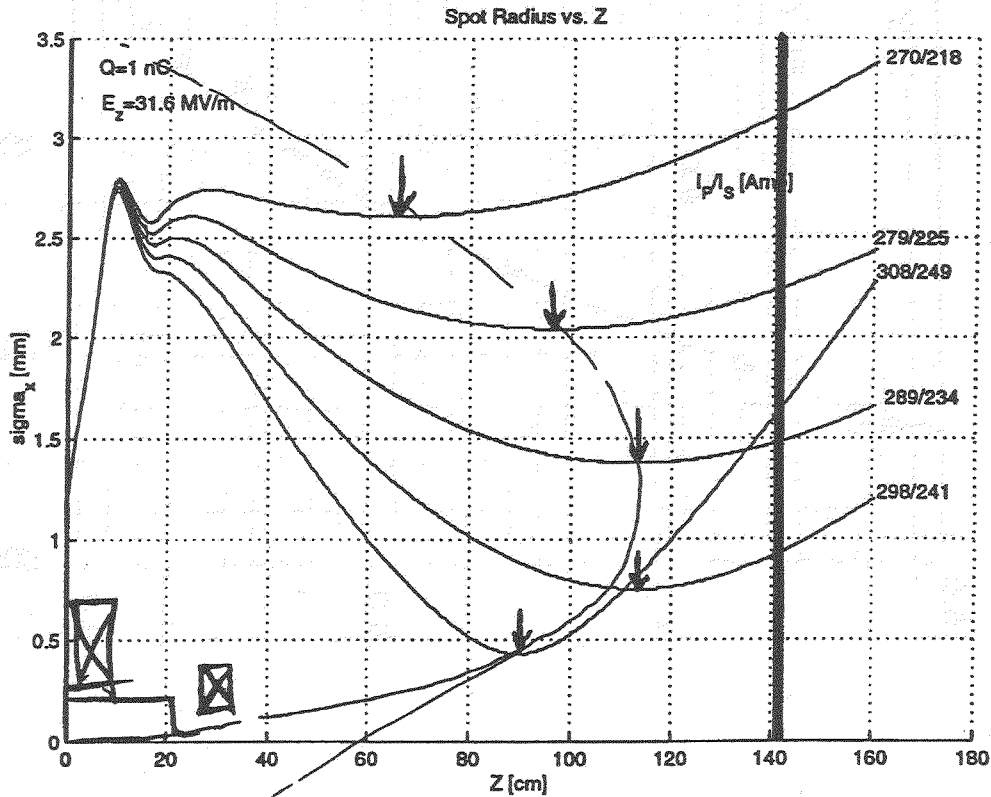
Figure 4.3. Position of the waist relative to the slits (PARMELA)

16

The Intensified CCD camera allows us to observe single bunches. We did three experiments with this camera using bunches separated by 1 µs in trains separated by 1 second.

The beam was observed on an OTR (Optical Transition Radiation) screen in cross 3. Some figures presented below show the intensity of the beam; the units for the intensity (counters) in these figures are given in Section 6.

5.1. First Experiment : 11/25-26/97

In this first experiment, we wanted to see the evolution of the intensity of each bunch in one train and the evolution of the dark current during the RF pulse.

On 11/25/97 we worked with 16 bunches and 1nC per bunch. We recorded 25 images in one RF pulse to have the 16 bunches and some values of the dark current before and after the bunch train. These images are in the folder ICCD 11/25/97 with the names bis#00 to ##24.

Figure 5.1 shows the intensity (with dark current) of each image. We can see that the first bunch appears at 3µs, followed by the missing second pulse, and the fourteen others.

On 11/26/97, we worked with 15 bunches and 1nC per bunch. We recorded 26 images of the dark current. Theses images are in the folder ICCD 11/26/97 with the names dark all time ##00 to ##25. The intensity as a function of time is shown in Figure 5.2.

Interpretation

In Figure 5.2, we see an increase in the intensity of the dark current during the RF pulse. This is because we accelerate the first bunch before the cavity reaches its equilibrium field level. This also explains why the first bunch in Figure 5.1 appears half as intense as the other bunches.
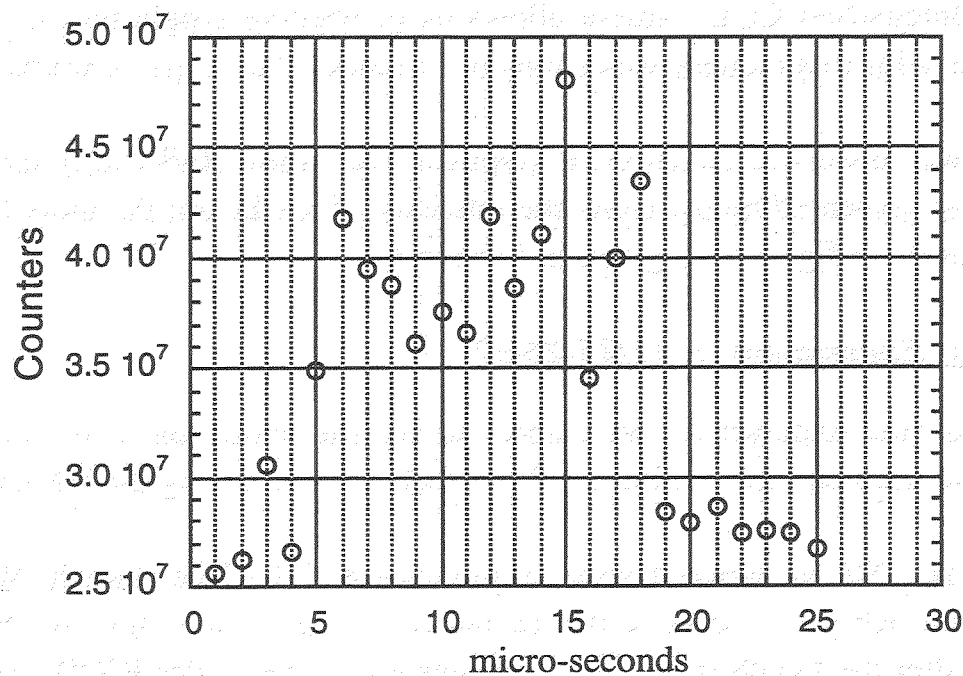
Figure 5.1. 16 pulses measured with the ICCD
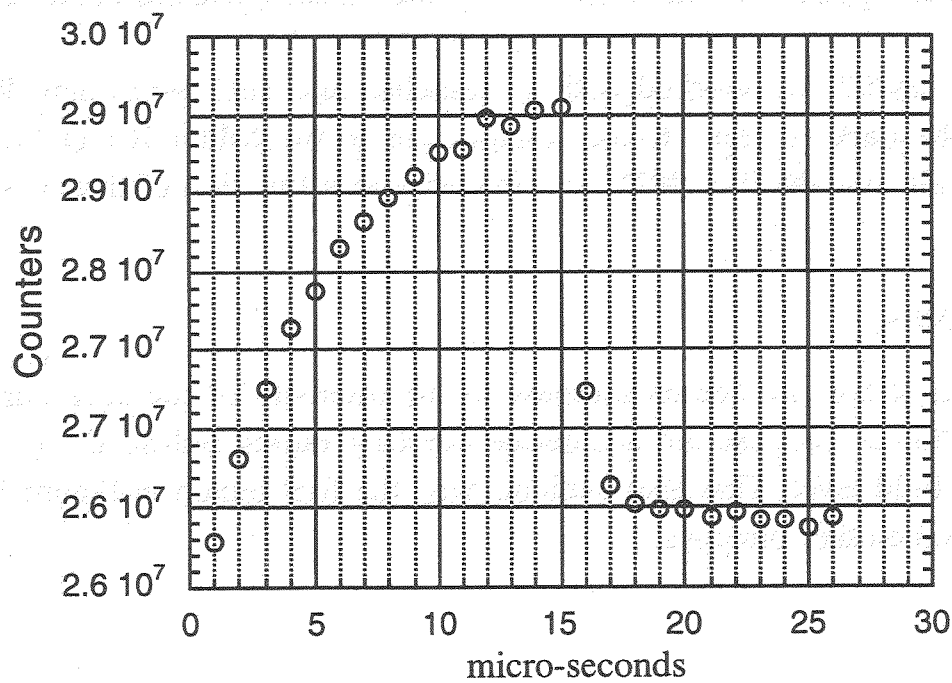
Figure 5.2. Dark current measured with the ICCD

5.2. Second experiment : 12/1

In this experiment, we wanted to see the evolution of the first bunch for 20 different trains (trains separated by 1 sec). We used 16 bunches (Figure 5.3) and we recorded the first bunch in each of 20 trains. We repeated this experiment 5 times for 5 different values of the charge measured with ICT1. Theses images are in the folder ICCD 12/1 with the names singlepulse1 to singlepulse5.

• Figures 5.4 and 5.5 show the evolution of the center of mass (respectively X and Y) as a function of the charge (with dark current).

• Figure 5.6 shows the evolution of the intensity as a function of the charge (with dark current).

• Figures 5.7 and 5.8 show the evolution of the widths σ_x (RMS X) and σ_y (RMS Y) as a function of charge (with dark current). The lowest value of the charge is not shown.

Interpretation

• In Figures 5.4 and 5.5, we can see a motion of the center of mass as a function of the charge. The motion seems linear for both X and Y.

• In Figure 5.6, we can see a linear increase in the intensity as a function of the charge, as expected, since the length of the bunches doesn't change when we vary the charge.

• In Figures 5.7 and 5.8, we can see an increase in the widths σ_x and σ_y as a function of the charge. Indeed, the space charge forces increase with the charge per bunch and produce an increase in the transverse dimensions of the beam.
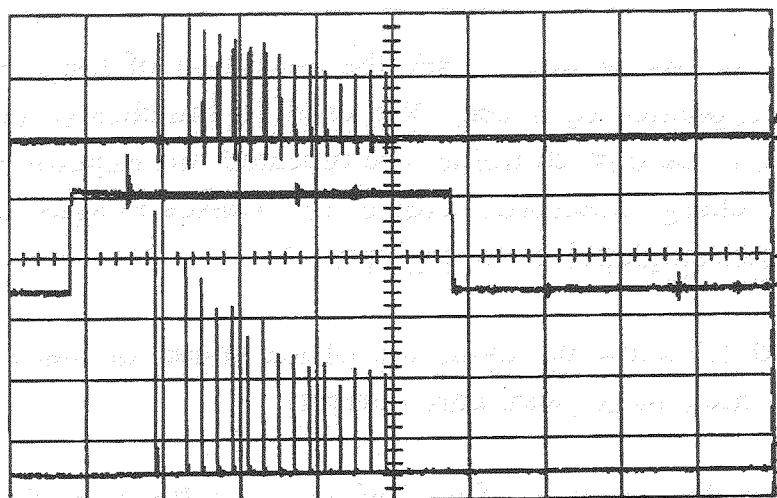
Figure 5.3. Pulse Train measured with the Le Croy scope
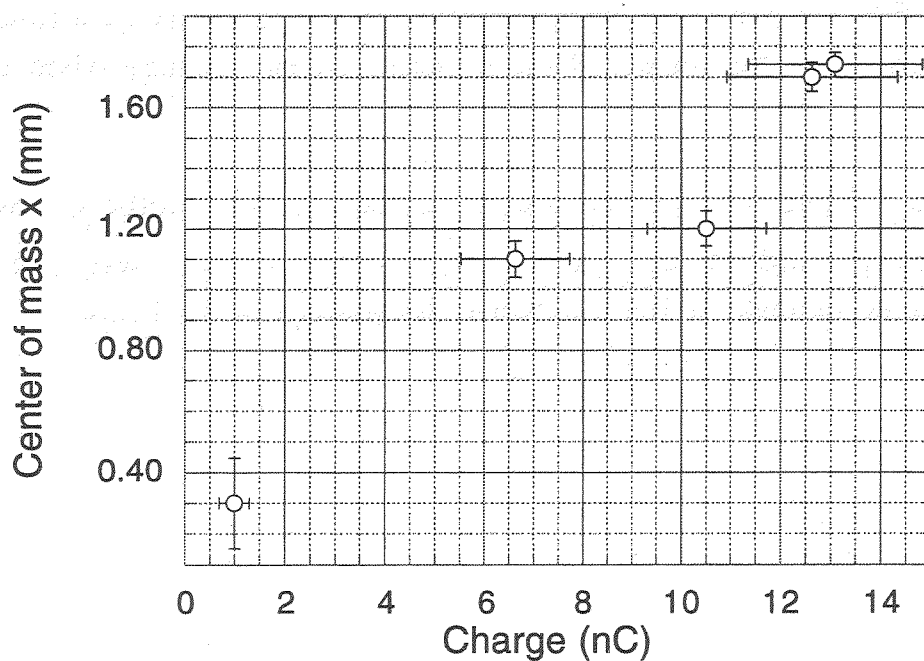
Figure 5.4. Center of Mass X versus the charge (ICCD)
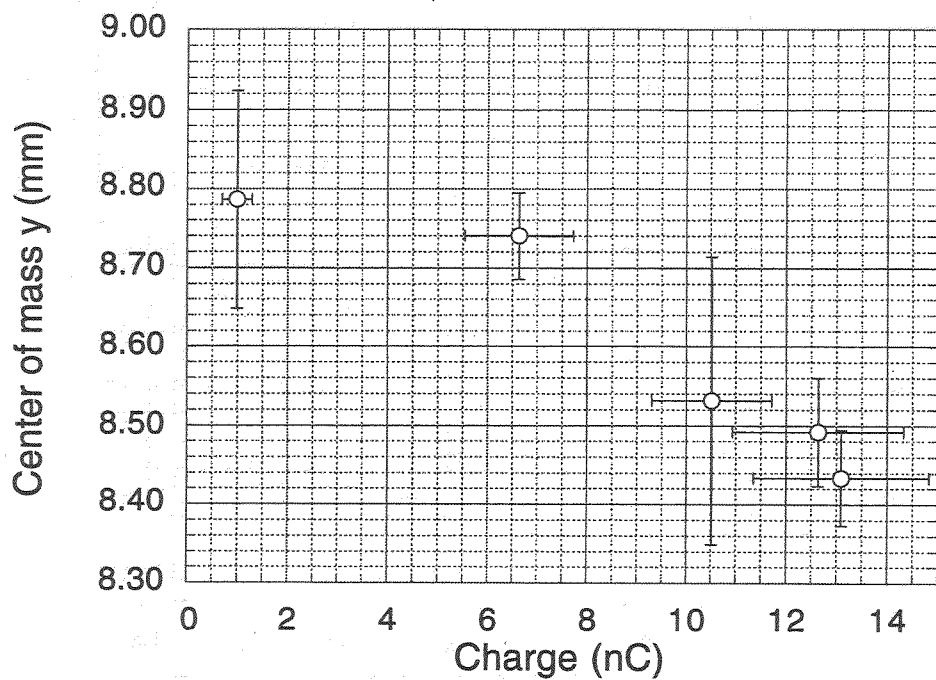
Figure 5.5. Center of Mass Y versus the charge (ICCD)
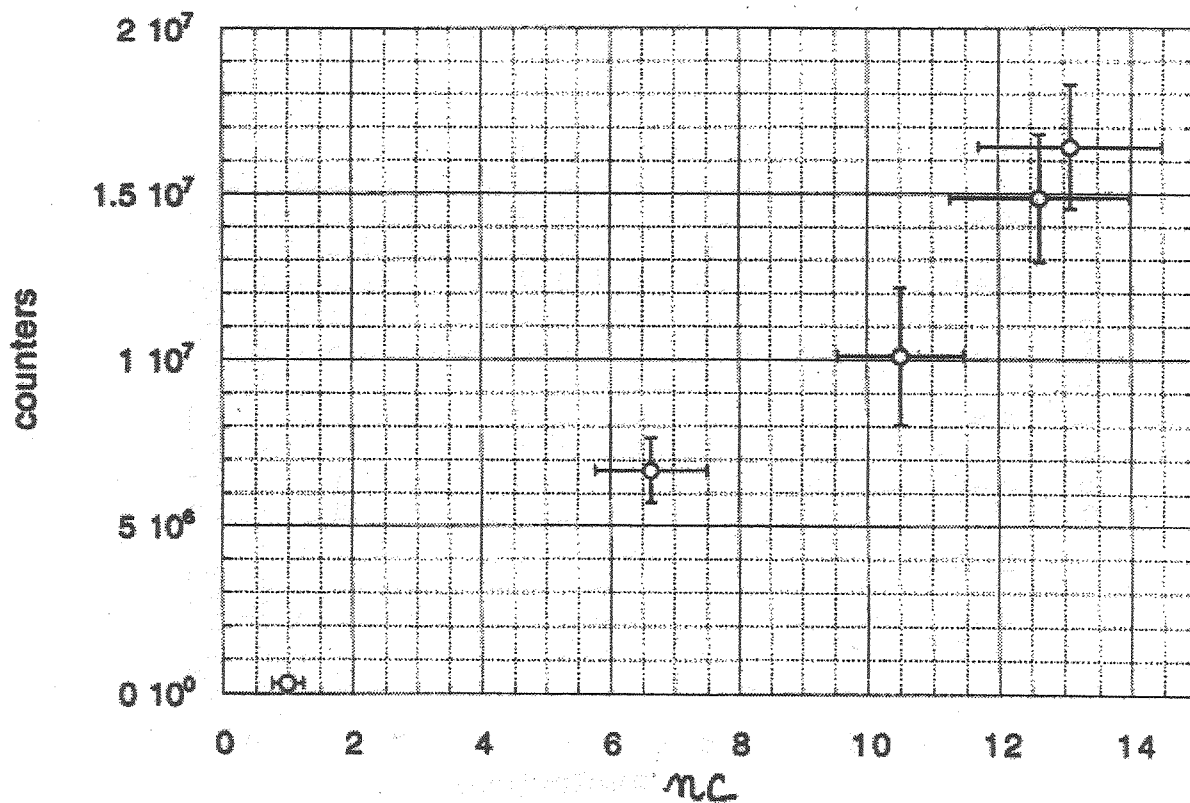
Figure 5.6. Intensity versus the charge (ICCD)

21
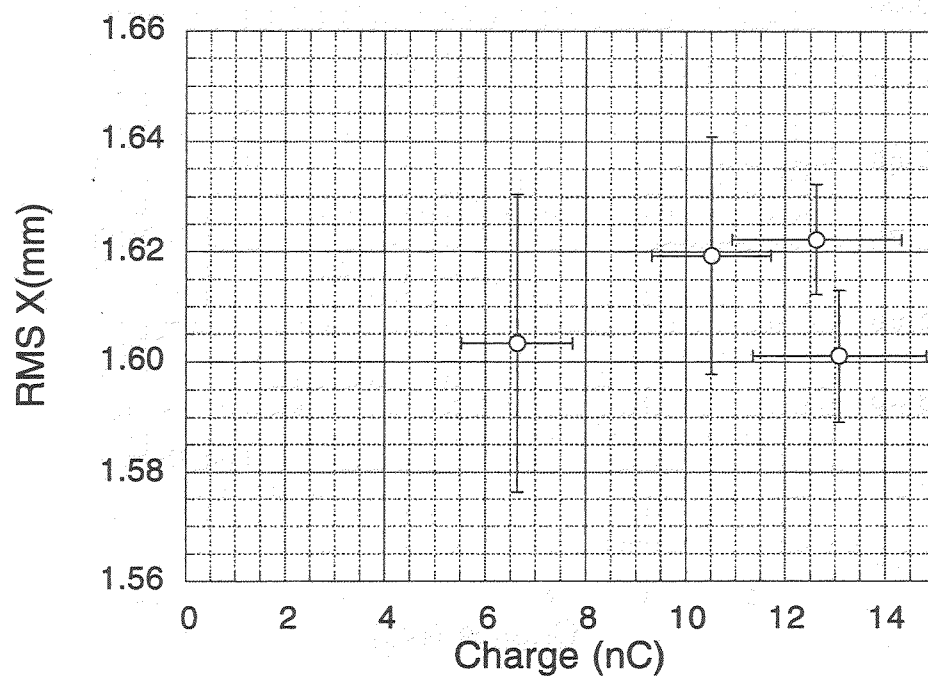
Figure 5.7. Spot size (RMS X) versus the charge (ICCD)
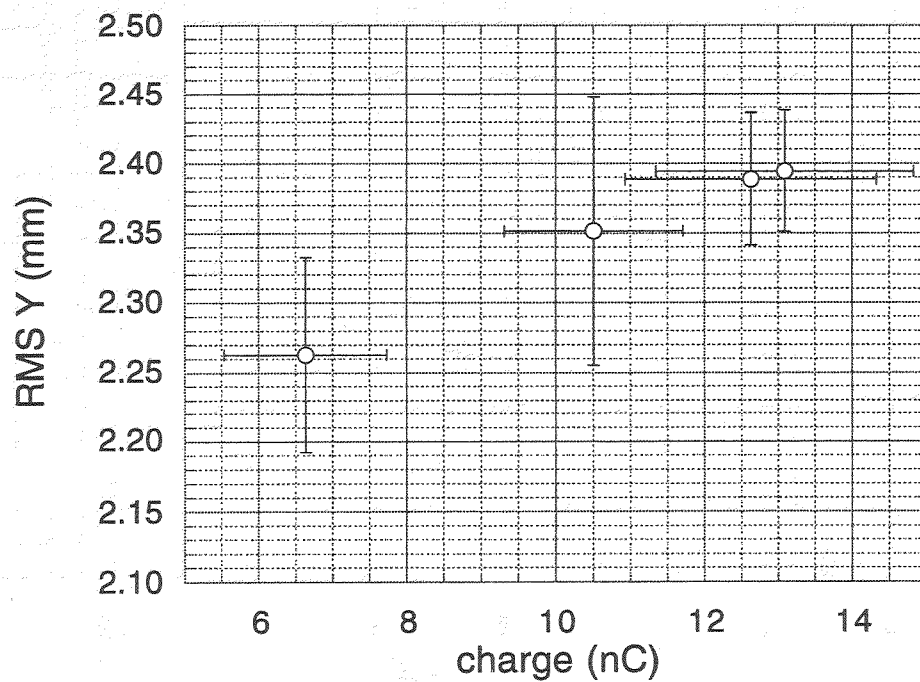
Figure 5.8. Spot size (RMS Y) versus the charge (ICCD)

5.3. Third experiment : ICCD 12/9

In this experiment, we wanted to analyze the evolution of all the bunches in the train. We worked with 15 bunches and 1nC per bunch. We recorded the first bunch in each of 20 different trains and we repeated this process for the second bunch (missing) of another 20 trains, continuing through the fifteenth pulse. We recorded also some images before and after the train to get some values of the dark current. These images are in the folder ICCD 12/9/97 /iccd stability / 6094#00 to 6118#19.

- Figure 5.9 shows the intensity of each bunch (with and without dark current).

- Figure 5.10 shows the intensity of the dark current i.e the same experiment as for Figure 5.9 but without the beam.

- Figure 5.11 and 5.12 show the evolution of the center of mass in X and Y respectively, for each bunch (dark current subtracted).

- Figure 5.13 shows a close-up of Figure 5.11 from the third bunch to the fifteenth bunch.

- Figure 5.14 and 5.15 show the evolution of the width σ_x (RMS X) and σ_y (RMS Y) for each bunch (dark current subtracted).

Interpretation

- Figure 5.9 and 5.10 show an increase in the dark current during the RF pulse. As we saw in § 5.1, the reason is that we accelerate the first bunch before the cavity is completely filled.

- The measurement of beam intensity (Figure 5.9), center of mass in X (Figure 5.11 & 5.13), center of mass in Y (Figure 5.12), all exhibit a 250 kHz (4µs) oscillation. These observations are consistent in that oscillations in beam intensity logically lead to oscillations in the beam's transverse position. A plausible explanation for the intensity oscillation is a 250 kHz amplitude modulation on the low-level RF drive to the klystron. The source of this modulation is not known at this time. Measurements will be necessary to locate the source, and a fix will have to be implemented.

• The last two Figures (5.14 and 5.15) show an increase in the beam size in the train. Indeed, the last bunches are larger in their transverse dimensions than the first one.
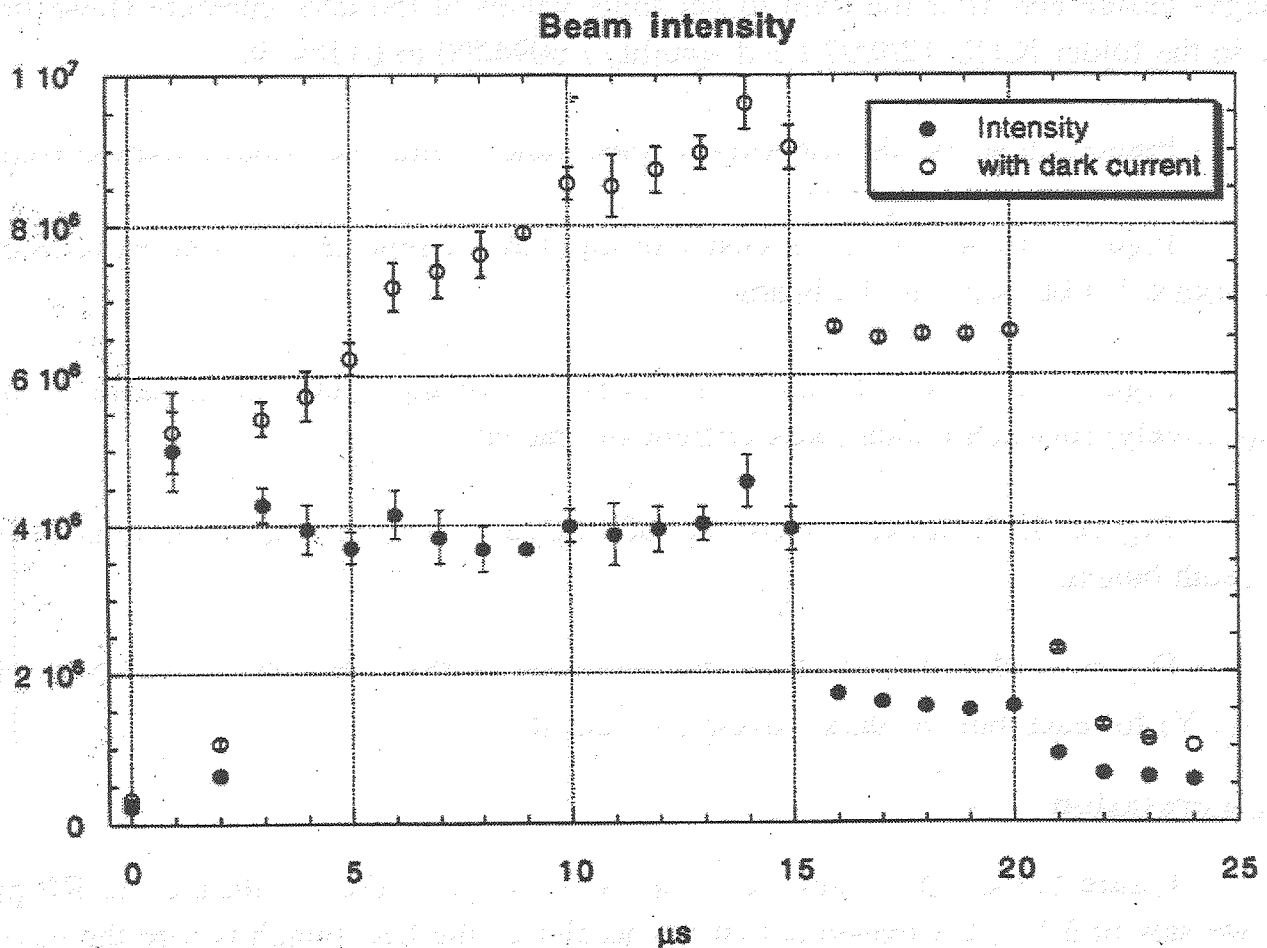
Figure 5.9. Beam intensity with and without dark current (ICCD)

Beam intensity
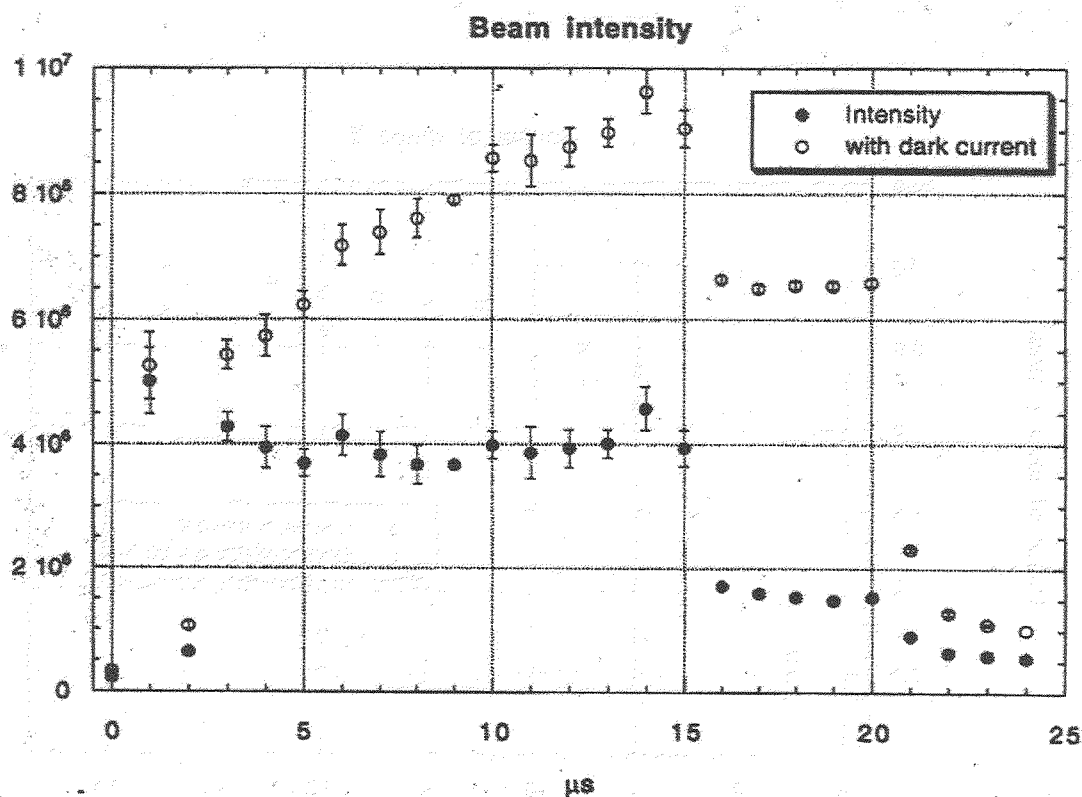
Figure 5.10. Dark current measured with the ICCD

com X
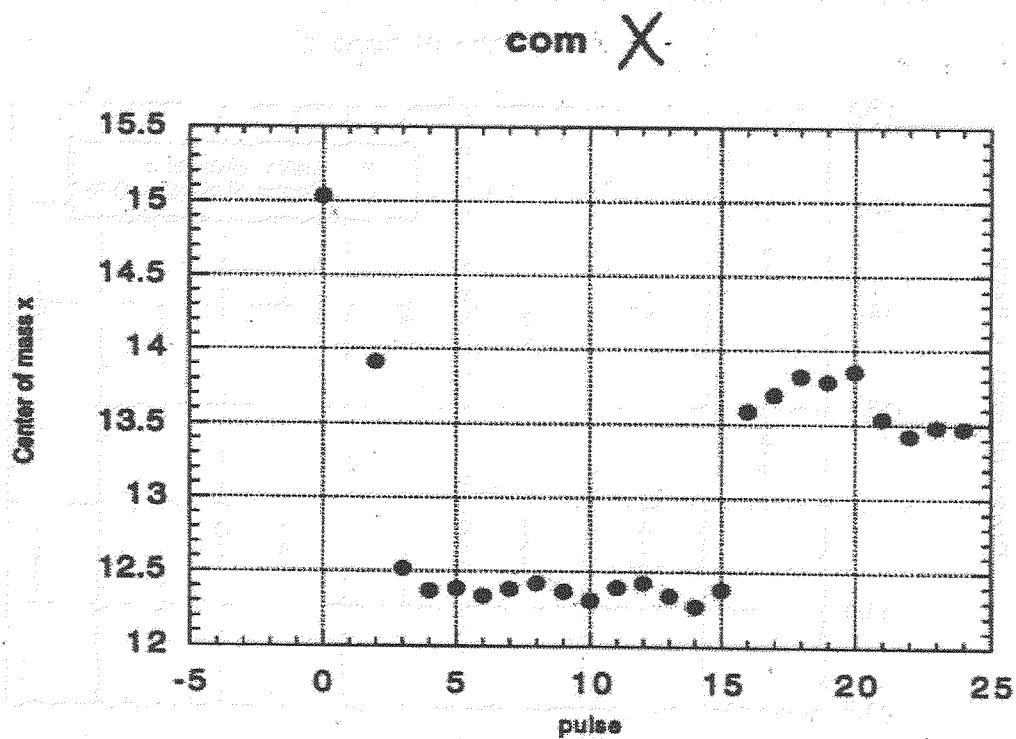
Figure 5.11. Center of Mass X measured with the ICCD
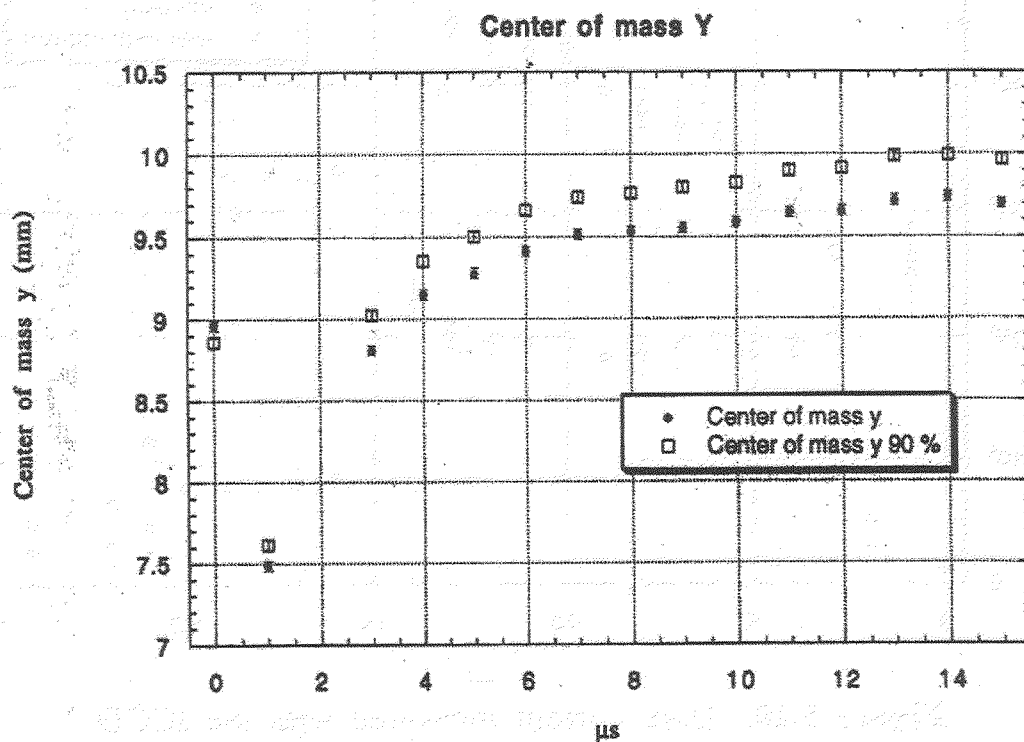
Figure 5.12. Center of Mass Y measured with the ICCD
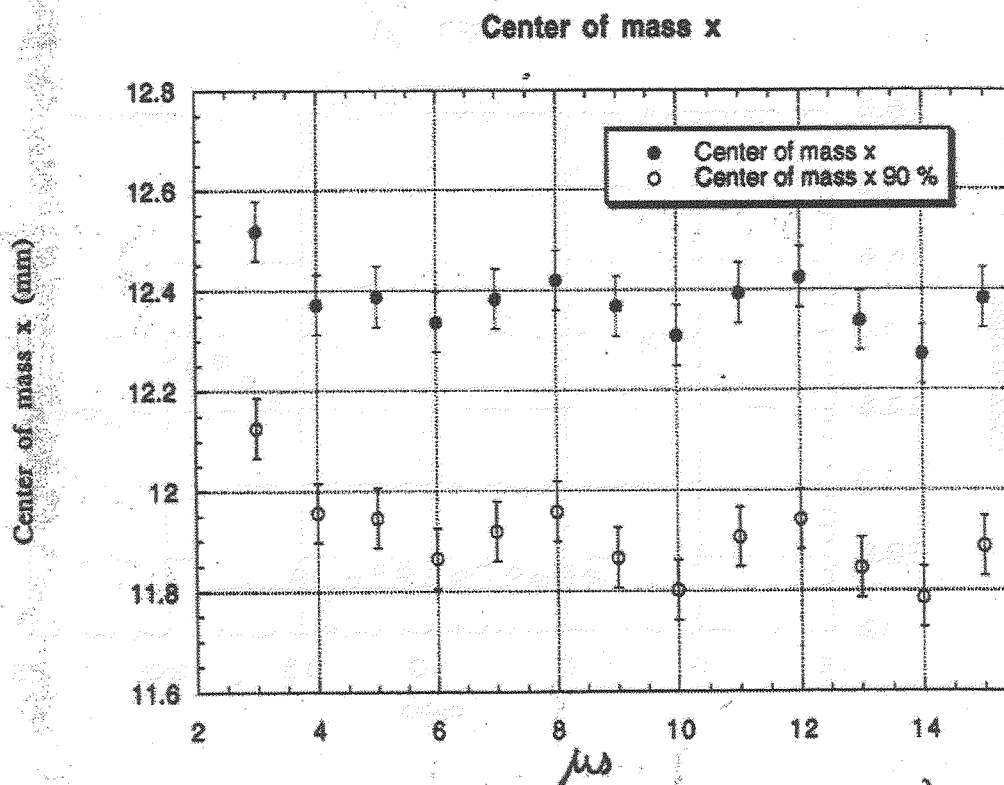
Figure 5.13. Center of Mass X (Zoom of figure 5.11)

RMSX
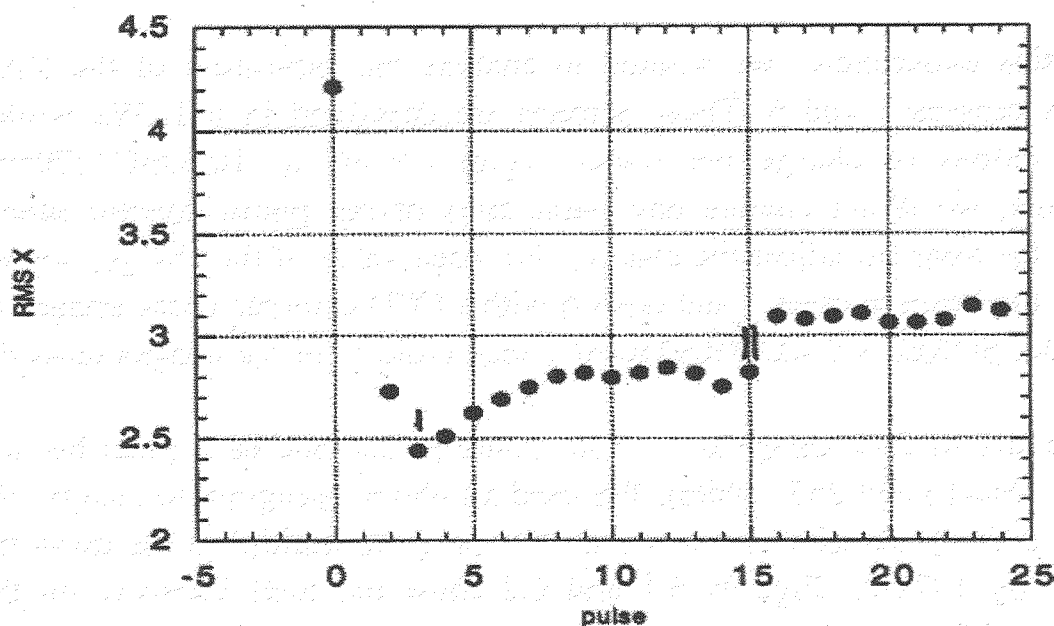
Figure 5.14. Spot size (RMS X) measured with the ICCD

RMSy
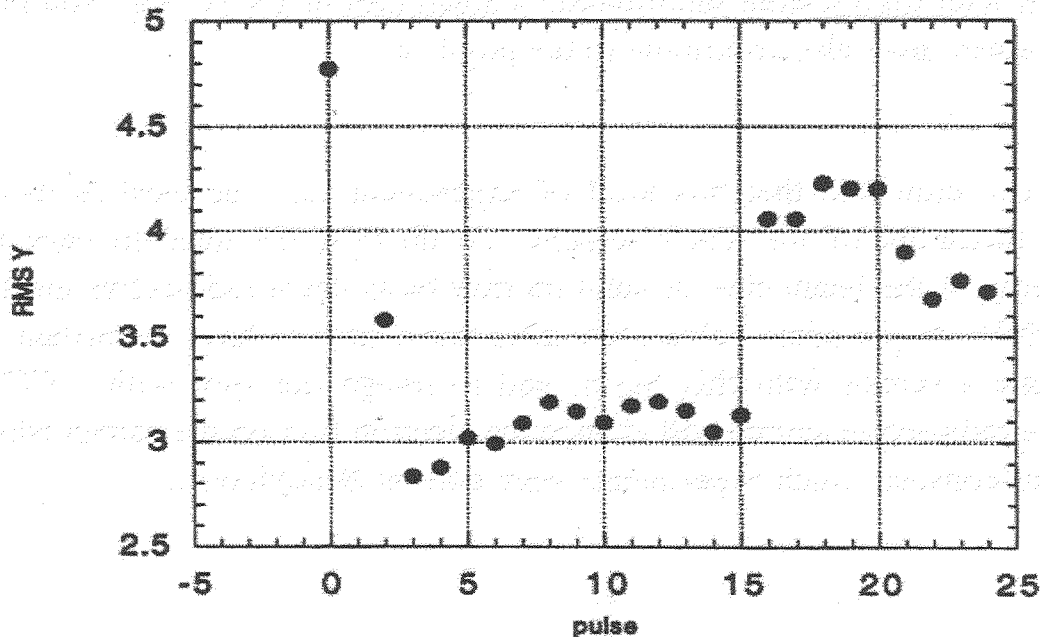
Figure 5.15. Spot size (RMS Y) measured with the ICCD

In this experiment, we wanted to analyze the saturation of the YAG screens located in crosses 5 and 6. These screens are described in § 1. We worked with 6 different values of charge per bunch, from 1.96nC to 10.59nC. During all the experiments, we didn't change any parameters of the photo-injector other than the energy of the laser (to adjust the charge). For each value of the charge, we recorded 50 images of the beam in cross 5 and cross 6 with a CCD camera. These images are located in the folder SCREEN CALIBRATION/ screen cross 4 (or 5)/ images cross 4 (or 5).

The size of each image is 107300 square pixels, and each pixel has an intensity between 1 (black) and 255 (white). We used a Labview program to analyze the images. To obtain the net intensity on the screen this program multiplies the mean intensity of the pixels by 107300. Figures 6.1 and 6.2 show the total intensity on the screens (screens 5 and 6 respectively) as a function of the amount of charge.

It can be seen that the total intensity on the screens is not linearly dependent on the charge. The main reason for this is that the beam size depends on the charge; a beam with less charge illuminating a large fraction of the screen can produce an intensity less that a beam with high charge illuminating a small part of the screen. Non-linearities in the CCD camera may also contribute to the problem.

We can conclude that this kind of experiment can't be used to determine the saturation threshold of the YAG screens. To do this, we need to vary the charge independently of the beam size. A solution may be to use a radioactive electron source (about 5 MeV), to put some collimators after this source to have a constant beam size, to illuminate a screen with this beam, and to image the spot with a CCD camera. Moving the radioactive source will change the electron flux on the screen while the spot size remains constant. Such experiments were done at Brookhaven.

Figure 6.1. Intensity in screen 4 for different charges
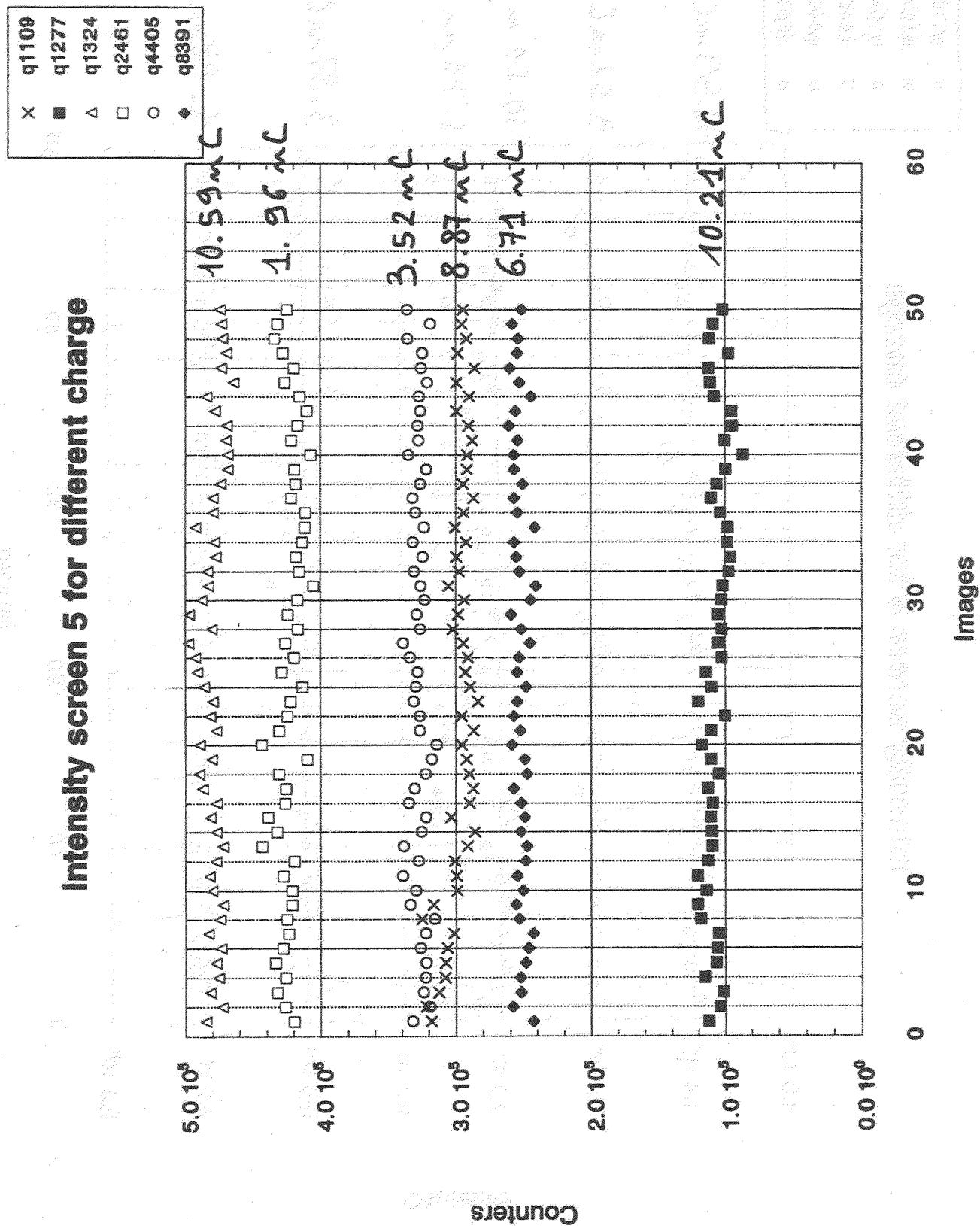
Figure 6.2. Intensity in screen 5 for different charges

30

In this experiment, the charge per bunch was measured with ICT1, ICT2, and a Faraday cup.

7.1. Faraday Cup Measurements

The charge per bunch can be measured destructively by intercepting the bunch with a "Faraday cup" and integrating the current directly. Faraday cups were placed at the end of both the straight and bent beam lines, after Crosses 5 and 6, respectively. The Faraday cups are sketched in Figure 7.1. Although quite different in hardware, both Faraday cups were intended to be electrically similar. As can be seen, in neither of the Faraday cups is the characteristic impedance matched between the incoming beam and the signal cable. Thus, there is the possibility of reflections and some distortion in the temporal structure of the bunch (additional distortion can be expected to occur as the signal pulse travels through the cable to the scope or integrator). Since the electrons are intercepted by a blank-off flange, we sometimes refer to these devices as "Faraday flanges."

Although a Faraday cup provides a direct measurement of the current, there are sources of systematic error. One source of error is secondary emission, *i.e.* low-energy electrons that are released from the Faraday cup when the high-energy electrons hit the surface. Since the secondary electrons are not generally collected, this results in an underestimate of the current. This problem can be cured by shaping the Faraday cup in such a way as to prevent the escape of secondary electrons. Another possibility may be to bias the Faraday cup. Neither of these cures was tried. Another possible source of error is transmission of the incident electrons through the Faraday cup. It is estimated that this was not a problem for the present measurements [4].

The hardware shown in Figure 7.1 was intended for measurements of the short photo-current bunches [5], although the dark current was also measured. The Cu shim of Figure 7.1a was intended to minimise the stray inductance. The resistors were intended to reduce the effect of the leads to the cable and decrease the peak signal voltage.

A simple circuit model for the Faraday cups is shown in Figure 7.2a. The beam current is represented by a current source $I_b(t)$; a voltage $V_s(t)$ is measured on the

(a)

- SS BEAM TUBE
- CERAMIC TUBE
- HOSE CLAMP
- Cu SHIM
- SS BLANK-OFF FLANGE (~150 mm OD, ~20 mm THICK)
- PHOTO-e⁻ BUNCH
- RESISTORS
- COAXIAL CABLE
- FC 1 SIGNAL

(b)

- G10 STRIP (3 AROUND CIRCUMFERENCE)
- HOSE CLAMP
- Ti FOIL (~80 μm THICK)
- SS BLANK-OFF FLANGE (~115 mm OD, ~17 mm THICK)
- PHOTO-e⁻ BUNCH
- RESISTOR (5 AROUND CIRCUMFERENCE)
- SS BEAM TUBE
- G10 TUBE
- COAXIAL CABLE
- RESISTOR
- FC 2 SIGNAL
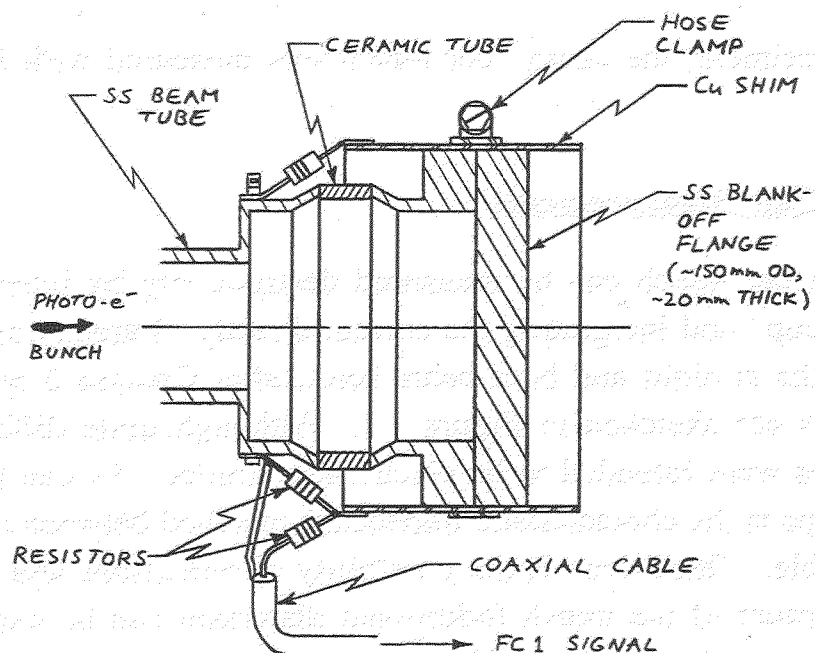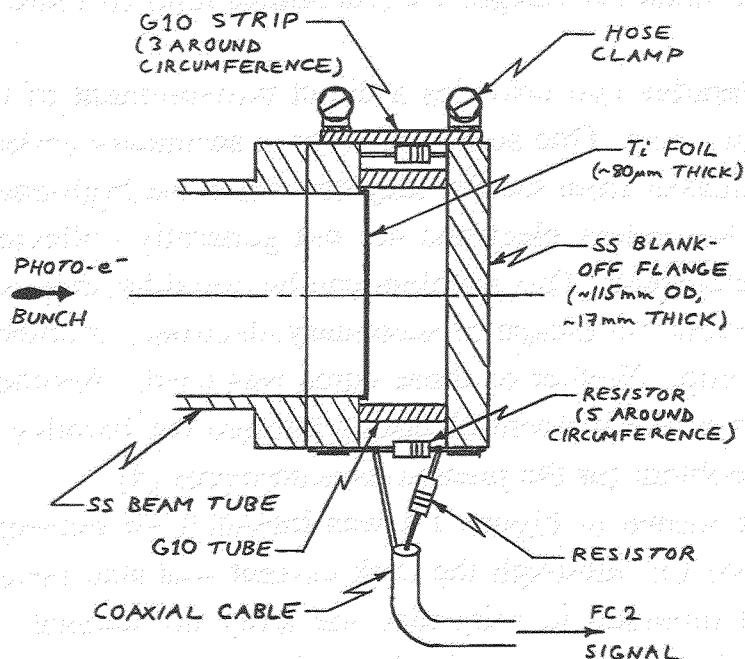
Figure 7.1. Sectional view of (a) the Faraday cup at the end of the straight beam line (FC1) and (b) the Faraday cup at the end of the bent beam line (FC2). Drawings are not to scale.

scope, which is terminated with $R_S = 50 \, \Omega$. The reality of several parallel resistors distributed along the circumference of the flange is represented by a single resistor R_G. Figure 7.2b shows a more complicated circuit model which includes a stray inductance L_F and a stray capacitance C_F. In the case of the simple circuit (Figure 7.2a), the beam current is related to the scope voltage via

$$I_b(t) = \frac{R_G + R_H + R_S}{R_S R_G} V_s(t) = Y_{FC} V_s(t) \tag{7.1}$$

where $Y_{FC} = \dfrac{R_G + R_H + R_S}{R_S R_G}$. Integrating over time, we get

$$\int_{-\infty}^{+\infty} I_b(t)\,dt = Y_{FC} \int_{-\infty}^{+\infty} V_s(t)\,dt \tag{7.2}$$

In the case of the more complicated circuit (Figure 7.2b), Equation (7.1) is not valid. However, if the voltages and currents are zero at the beginning and the end, as is the case for a pulse of beam current, Equation (7.2) is also applicable to the complicated circuit. Thus, if we take the area of the voltage pulse measured on the scope, we do not need to take into account the stray inductance and capacitance.[1] So we can deduce the charge Q_b per bunch via

$$Q_b = Y_{FC} \int_{-\infty}^{+\infty} V_s(t)\,dt \tag{7.3}$$

We also expect that, by using the area of the Faraday cup signal, we can minimise the effect of the cable attenuation on the result (see § 8.1). The background area, if any, must be subtracted, however.

For the Faraday cup in the straight beam line (FC1), it is believed that we had $R_H = 500 \, \Omega$ and $R_G = 50 \, \Omega$; for the Faraday cup in the bent beam line (FC2), we believe we had $R_H = 521 \, \Omega$ and $R_G = 48 \, \Omega$ (the latter consisting of five parallel

---

[1] However, the capacitance and inductance form a resonant circuit, which opens up the possibility of unwanted ringing in the Faraday cup signal for an unhappy combination of L_F, C_F, and R.

(a)
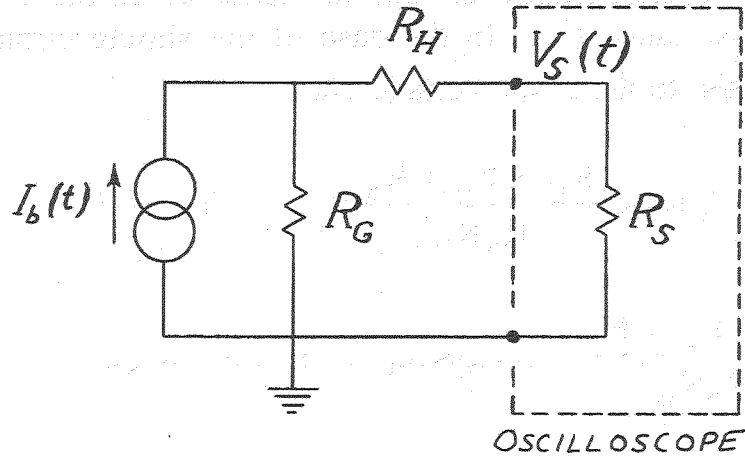
(b)
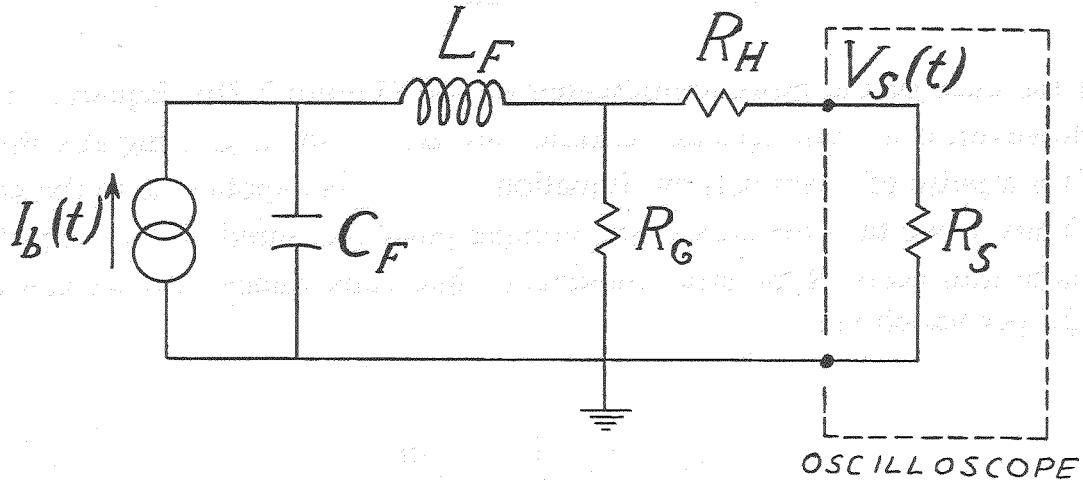
Figure 7.2. (a) Simple and (b) complicated circuit models for a Faraday cup.

resistors, each 240 Ω). With a scope impedance R_S of 50 Ω, we obtain $Y_{FC} = 0.24$ Ω^{-1} for FC1 and $Y_{FC} = 0.258$ Ω^{-1} for FC2. No checks of the performance of the Faraday cups have been done, however.

7.2. *ICT Measurements*

The charge per bunch can be measured non-destructively with integrating current transformers (ICT's) [6]. Commercially-available ICT's of French manufacture were used [7]. ICT1 (serial number 242) was at the exit of the gun; ICT2 (serial number
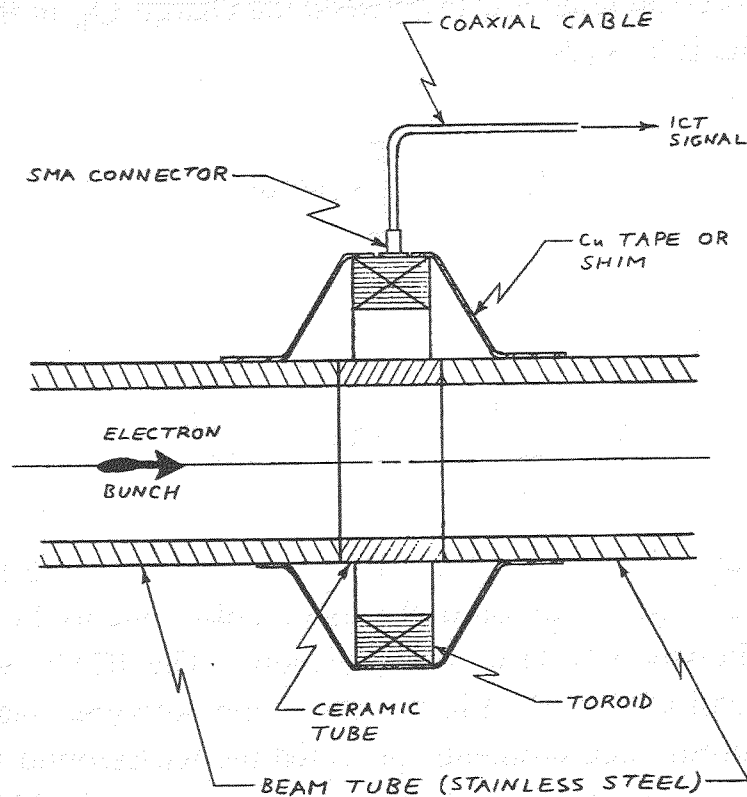
Figure 7.3. Sectional view of ICT toroid on beam line (not to scale).

219) was between Cross 2 and Cross 3. The model number for both ICT's was ICT-122-070-20:1.

As shown schematically in Figure 7.3, the ICT consists of a toroid placed outside the vacuum chamber. A pulse of current passing through the toroid produces a signal pulse; in principle, the integral of the signal voltage over time is proportional to the charge in the current pulse. The beam's image current travelling along the beam pipe must be diverted around the outside of the toroid by interrupting the conducting beam tube with an insulating ceramic and providing a path for the image current to travel outside the toroid (see Figure 7.3). Cu tape was used to do this in the present experiments, although a more complete shield is recommended [7] to minimise noise pick-up.[2]

The turns ratio is 20 to 1 for both ICT's. If the input impedance of the scope (or integrator) is 50 Ω, the net impedance seen by the signal (internal plus scope) is 25 Ω.

---

[2] In future experiments, the ICT shielding will be done via a piece of Cu shim with ends attached to the beam tube by hose clamps.

In this case, the theoretical relationship between the charge Q_b in the bunch and voltage pulse $V_s(t)$ from the ICT is [7]

$$Q_b = Y_\gamma \int_{-\infty}^{+\infty} V_s(t)\,dt \qquad (7.4)$$

with

$$Y_\gamma = \frac{20}{25\Omega} = 0.8\Omega^{-1} = \frac{0.8C}{V.s} \qquad (7.5)$$

The above applies for input pulse durations of up to about 2 µs. For input pulses longer than about 2 µs, there is droop in the signal pulse (due to the internal capacitance of the toroid) and Equation (7.4) is not applicable. The ICT's were checked with a pulse generator, as will be described in Section 8; the outcome was that Equation (7.4) is valid for photo-current measurements, provided the background is subtracted and, in the case of ICT1, provided the solenoid fields do not saturate the ICT.

7.3. Experiment

Comparative measurements of the ICT1, ICT2, and FC1 signals were done for 1 bunch on 2 October 1997. The solenoids were operated at reduced field, with the hope of getting an accurate reading from ICT1: the current was 80 A in the primary solenoid, 97 A in the secondary solenoid, and 59 A in the trim solenoid. An example of the scope traces is given in Figure 7.4. As expected, the duration of the signal pulses is long compared to the bunch length, since it is determined by the response time of the device and the distortion from the cable. The negative area of the Faraday cup signal is consistent with the negative charge of the electron bunch; the ICT signal areas are positive because the ICT's were installed backwards.

The area of the signal pulse was obtained directly with the scope, after averaging over a number of RF pulses. The same bunch in the train was used on every RF pulse. The background area was not subtracted; this can be expected to produce some systematic error, although the base-line levels for all 3 signals were quite close to zero at the time of the measurements. Charge values deduced from Equations (7.3) and (7.4) are given in Table 7.1. As can be seen, if we exclude the case in which the beam was

36
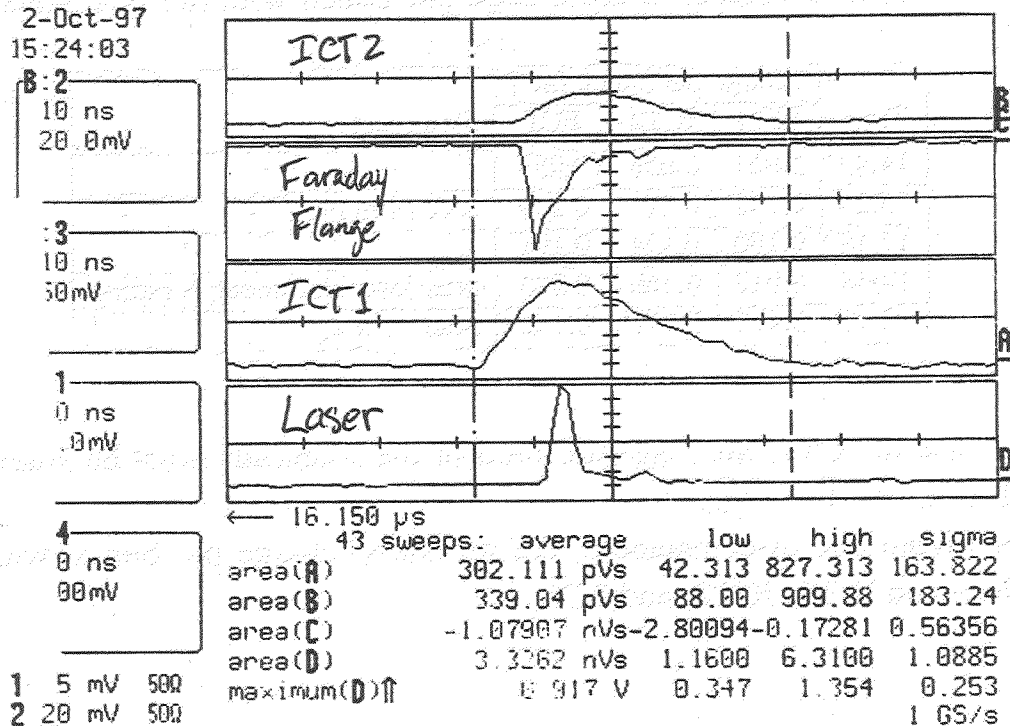
Figure 7.4. Scope traces of the ICT1, ICT2, and FC1 signals produced by 1 bunch of photo-electrons. The horizontal axis is time (10 ns per division). The laser pulse signal is also shown.

scraping the beam tube, the measured values of the charge per bunch from the 3 different sources agree within 12%.

7.4. *Summary*

To measure the charge per bunch with one of the Faraday cups, we want to take the area of the Faraday cup's voltage signal, with 50 Ω input impedance for the scope or integrator, and subtract the background area. We obtain the charge via Equation (7.3), using $Y_{FC} = 0.24$ Ω^{-1} for FC1 (at the end of the straight beam line) or $Y_{FC} = 0.258$ Ω^{-1} for FC2 (at the end of the bent beam line).

To measure the charge per bunch with one of the ICT's, we want to take the area of the ICT's voltage signal, with 50 Ω input impedance for the scope or integrator, and subtract the background area. We obtain the charge via Equation (7.4), with $Y_{\gamma} = 0.8$

Table 7.1. Measurements of the charge per bunch with the ICT's and FC1.

Time	Charge per bunch [nC]			Comments
	ICT1	ICT2	FC1	
14:43	0.054	0.056	0.053	
15:24	0.242	0.271	0.259	data from Fig. 7.4
17:18	0.180	0.194	0.191	
17:48	0.912	0.360	0.326	after laser alignment; scraping
18:18	0.475	0.471	0.442	after steering

Ω^{-1}. In the case of ICT1, the magnetic field of the solenoids must be small enough to avoid an effect on the ICT signal.

Under favourable circumstances, the measured charge per bunch was consistent up to 12% between ICT1, ICT2, and FC1.

As described in § 7.2 and shown in Figure 7.3, the charge per bunch was measured with two ICT's. The ICT's were also used to measure the dark current produced by the RF gun. The behaviour of the ICT's was checked with a pulse generator, as will be described in this section.

8.1. Measurement of the Photo-Current

The duration of the photo-current bunch is not known precisely, but it is believed to be between 1 and 10 ps, depending on the laser pulse duration and the longitudinal emittance growth due to space charge. Thus Equation (7.4) is valid. The ICT signal produced by a photo-electron bunch is shown in Figure 8.1. As can be seen, the duration of the signal pulse is much longer than 10 ps. This is consistent with the manufacturer's specification [7], which is that the frequency content of the ICT signal is independent of the input pulse duration if the latter is less than about 5 or 10 ns, and that the signal pulse has a rise time of about 20 ns under these circumstances (with a 6σ duration of about 70 ns). Since the time interval between successive bunches within one train is 1 μs, there is ample time for the signal pulse from one bunch to decay before the arrival of the next bunch.

The voltage signal was integrated either "by hand" from the printed scope trace or via the signal integration capability of the digital scope. There is typically an offset or background signal (as can be seen in Figure 8.2, for example) due to dark current, cross-talk with the modulator, or what-not. In the case of integration by hand, the area of the signal alone can be calculated; in the case of integration with the scope, the background must be subtracted explicitly.

Calibration Checks with Pulse Generator

The ICT's were checked with a pulse generator using the scheme shown in Figure 8.2. The pulse from the generator passes through the ICT and is viewed on a scope, along with the signal pulse from the ICT. A scope input impedance of 50 Ω is used for both channels. In the configuration shown in Figure 8.2, the measurement can be done without disrupting the vacuum system. If the ICT is not already on the beam line, the actual geometry can be better approximated by including a short section of beam tube with ceramic break, connecting the ground wires to the beam tube, adding a conducting

9:50:58

50 ns
20.0mV

1
50 ns
100mV

1 = laser diode

4 = ICT 1

$I_{\mu i} = 240\ A$

$I_{rec} = 95\ A$

$I_{aim} = 95\ A$

ICT#1

4

1

⟵ 33.525 μs

pkpk(1)   166mV
pkpk(4)   48.7mV
maximum(4)   41.2mV
maximum(1)   165mV

$P_f \gtrsim 360\ mV$

50 μs pulse

1 Hz rep rate

1 .1 V 50Ω
2 50 mV 50Ω
3 .1 V 50Ω
4 20 mV 50Ω

⌐_ Ext DC 405mV 50Ω

500 MS/s

☐ STOPPED
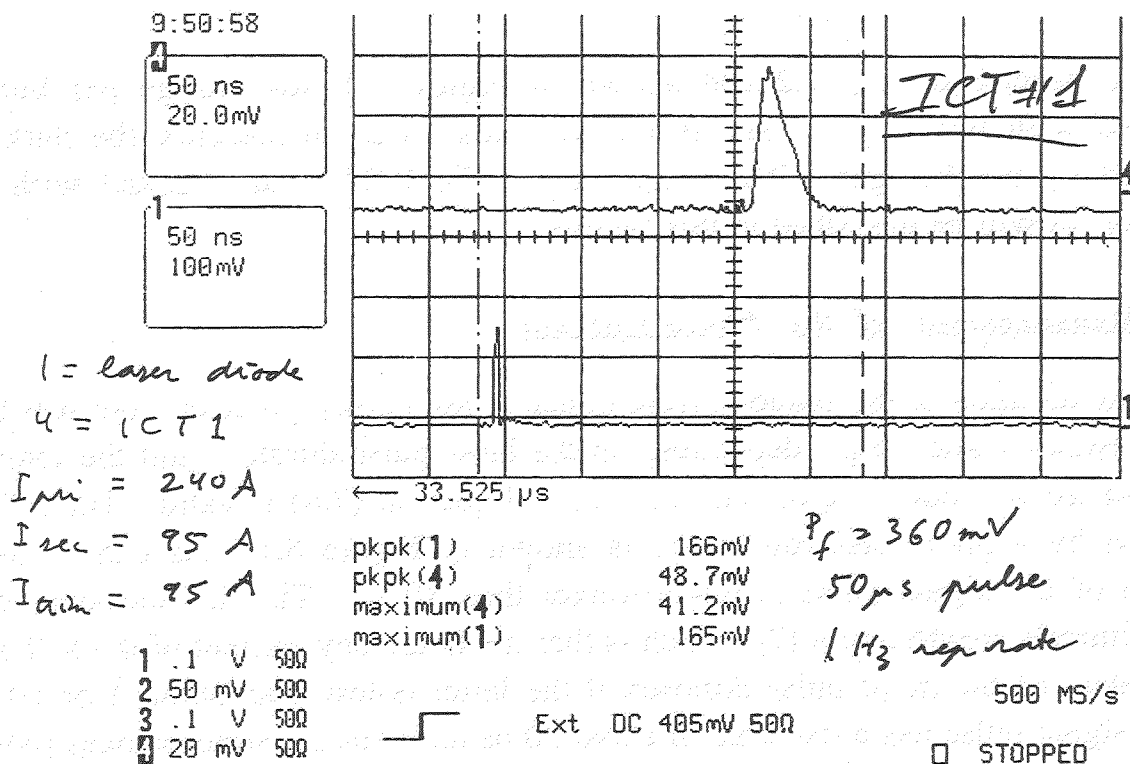
Figure 8.1. Scope traces of the ICT signal produced by 1 bunch of photo-electrons (top) and the laser signal (bottom). The horizontal axis is time (50 ns per division). The vertical axis is voltage (20 mV per division for the ICT signal). The zero volts level is indicated by the bar under the "4" on the right edge of the display.

path for the image current, and passing the inner wire through the beam tube (cf Figure 7.3). The transition from coaxial cable to wire can be made abruptly (adapter from BNC to alligator clip leads) or more smoothly. In the case of an abrupt transition, there is the possibility of some reflection of the drive pulse between the generator and the scope.

A series of measurements were done on a third ICT (serial number 291) with a pulse generator to check the behaviour. A ceramic break and Cu tape were used to try to mock up the actual geometry, as sketched in Figure 8.3. Figure 8.4 shows the ICT signal pulse produced by a drive pulse with a duration of about 2 ns. The drive pulse is also shown, both sent directly to the scope (the "direct" pulse) and sent through the ICT first and then to the scope (the "through" pulse). As expected, the rise time of the
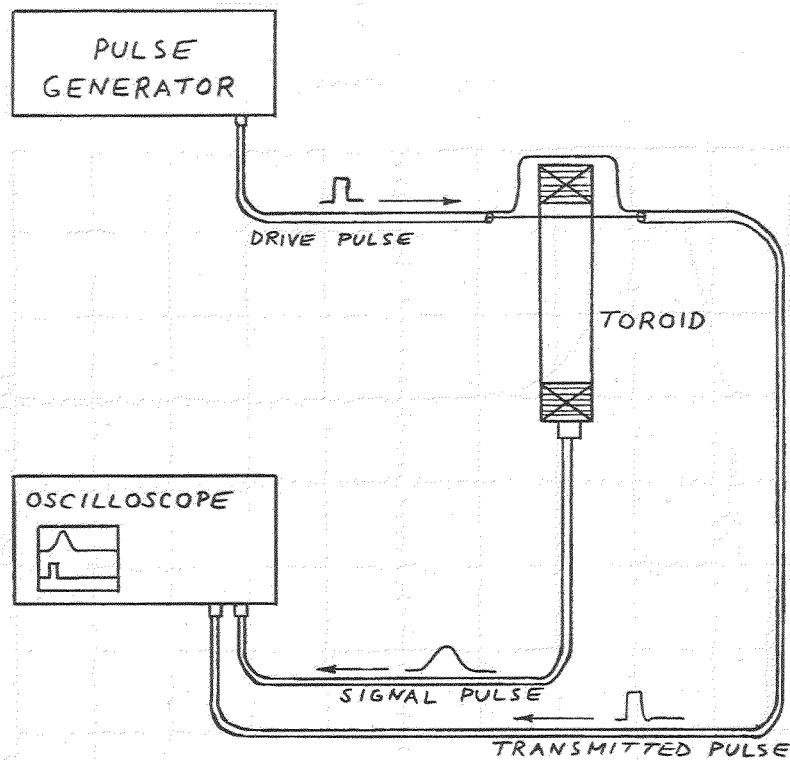
Figure 8.2. Configuration for checking an ICT with a pulse generator.
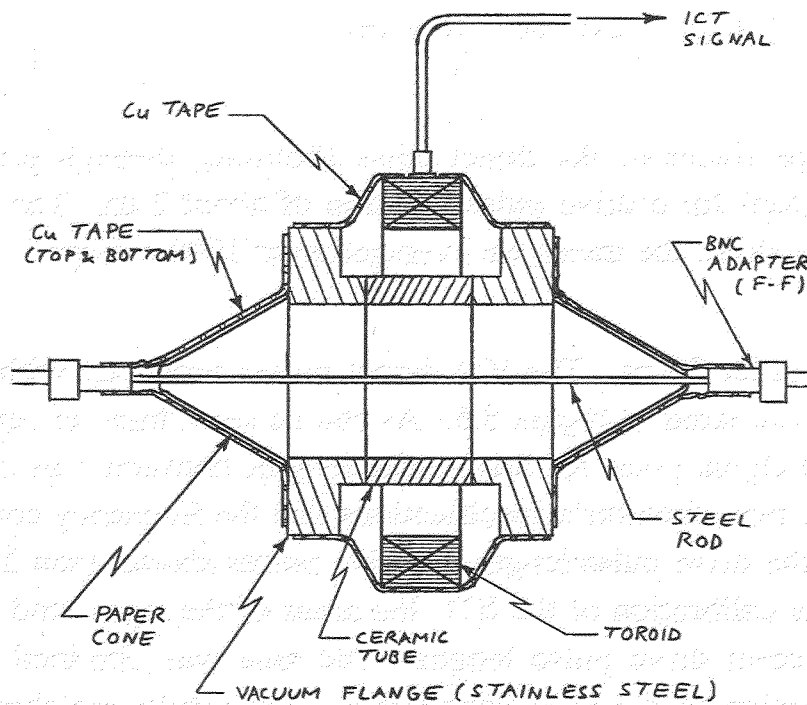
Figure 8.3. Scheme for pulse generator measurements with reduced reflections.

41
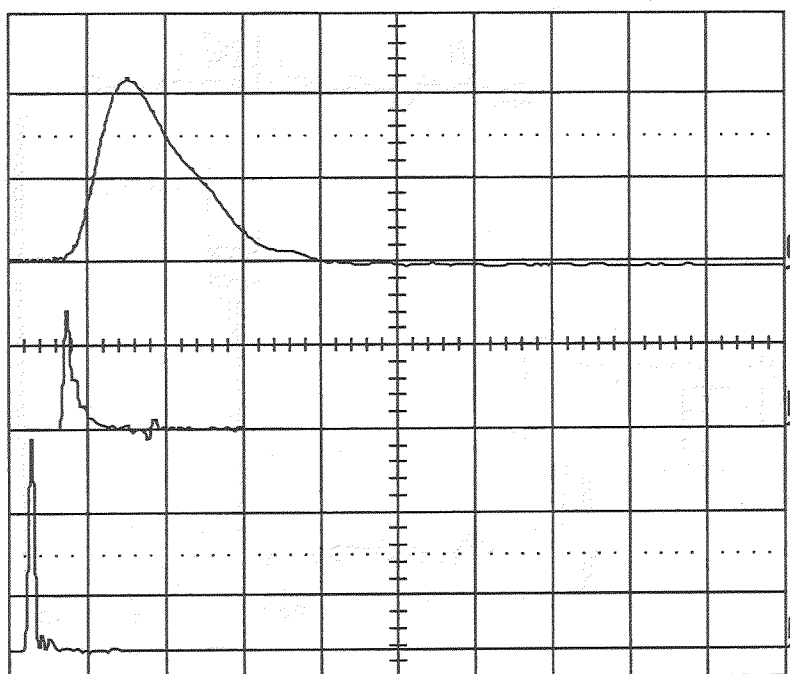
Figure 8.4. Scope traces of the direct pulse (bottom), through pulse (middle), and ICT signal pulse (top) for a drive pulse duration of about 2 ns. The horizontal axis is time (20 ns per division); the traces are averaged over 1000 sweeps.

signal pulse is of order 20 ns. The ICT signal pulses produced with 4 different drive pulse lengths are compared in Figure 8.5. As can be seen, there is very little difference in the shape of the signal pulse for drive pulse lengths between 2 ns and 15 ns. This is consistent with the manufacturer's specifications that the frequency content of the signal is independent of the drive pulse length for drive pulses shorter than 5 or 10 ns.

To check the calibration of the ICT, the areas of the signal and drive pulses were measured for different drive pulse lengths. The area was obtained directly with the scope, with subtraction of the background area. The results are shown in Figure 8.6. The area of the drive pulse is slightly smaller after it travels through the ICT, presumably due to reflections. This represents an uncertainty in the measurement---the area of the pulse that actually travels through the toroid can be expected to be
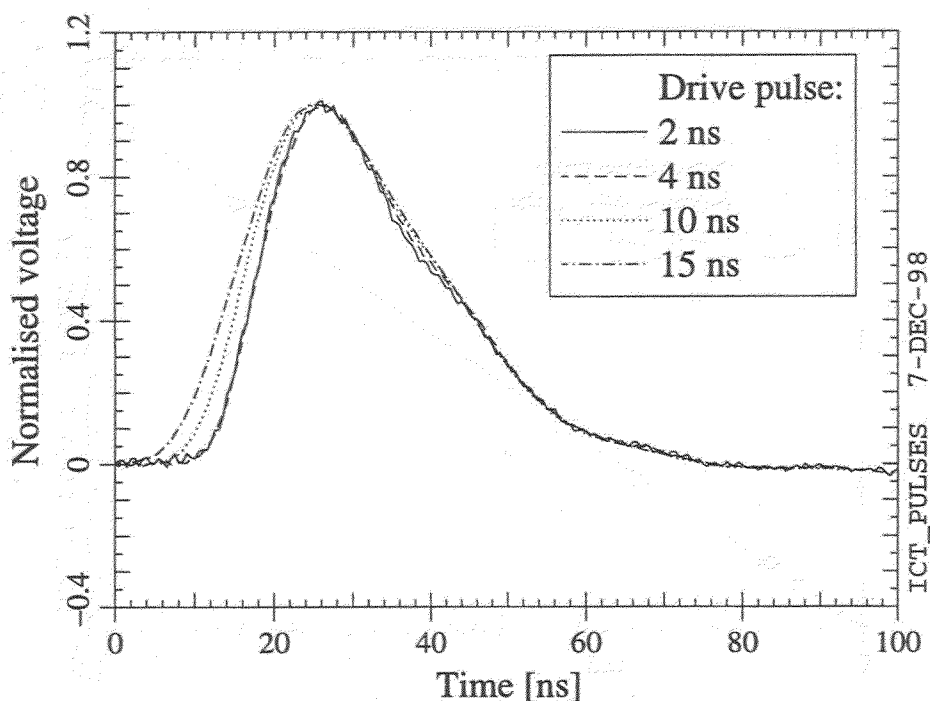
Figure 8.5. Comparison of ICT signal pulse shapes for 4 different drive pulse lengths. In order to get the most overlap, the amplitude is offset to 0 and normalised to for all pulses and the time offsets are adjusted.

somewhere between the areas of the direct and through pulses. With this uncertainty i mind, the measurements are consistent with the theoretical relationship of Equation 7. represented by the solid line in Figure 8.6. The ratio of signal pulse area to drive pul area is relatively constant over the measured range of drive pulse lengths (2 ns to ns).

Measurements were also done with simple BNC to alligator clip transitio without any attempt to mock up the geometry of the beam tube. Figure 8.7 sho various signal pulses produced by holding the wires in different positions. The sig pulse is significantly distorted, although the area of the signal pulse does not cha much. Somewhat larger distortion in the signal was seen with ICT2 (serial num 219). Nevertheless, the ICT's can be checked in situ with just alligator clips; it is necessary to mock up the geometry in order to check whether the toroid is working.

43
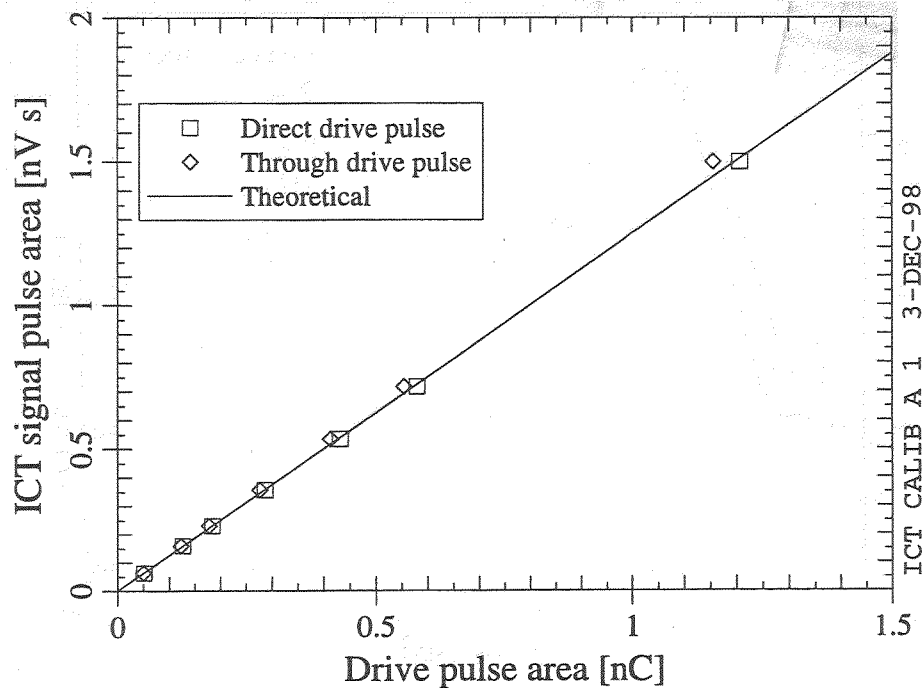
Figure 8.6. Measured pulse areas for different drive pulse lengths, from 2ns to 40ns.

Cable Attenuation

The pulse generator measurements described above were done with a short cable from the ICT to the scope, namely an RG58 cable with a delay of 8 ns and BNC connectors. However, for photo-current measurements, relatively long cables are required to bring the ICT signals from the bunker to the scope outside. The long cables were also RG58, which has a relatively high attenuation per unit length. Measurements were done to quantify the effect of the cables on the ICT signal pulse.

The length of the cables was determined via an S_{11} measurement with a network analyser. The cable delays were deduced to be 225.3 ns for the ICT1 cable and 225.8 ns for the ICT2 cable.

Cables of type RG58 of about the same length were used for the Faraday cup signals. The present discussion will therefore also apply to the Faraday cups.

5-Dec-98
19:22:01

A:Average(3)
20 ns
8.0mV
1000 swps

B:Average(3)
20 ns
8.0mV
1000 swps

C:Average(3)
20 ns
8.0mV
1000 swps

D:Average(3)
20 ns
8.0mV
1000 swps

20 ns

← 8 ns

A
B
C
D
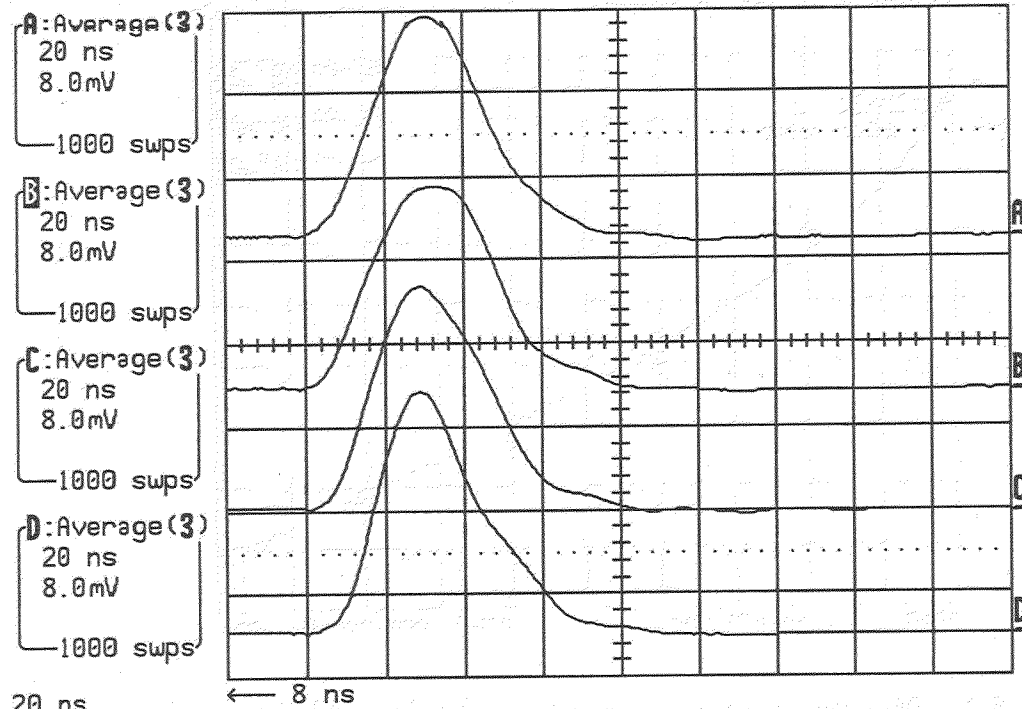
1 disabled
2 1 V 50Ω
3 10 mV 50Ω
4 disabled

Ext DC -410mV 1MΩ

2 GS/s

NORMAL

Figure 8.7. ICT signal pulses for 4 different positions of the wires for the drive pulse relative to the toroid.

Frequency Domain

The individual attenuations of each of the two cables could not be measured easily, since the cables were already installed in cable trays. Instead, the attenuation of the 2 cables in series was measured by connecting them together inside the bunker and connecting the other ends to a network analyser outside the bunker. Figure 8.8 shows an S_{21} measurement of the 2 cables. As expected for RG58 cable, the attenuation increases rapidly with frequency. Since the rise time of the signal pulse is of order 20 ns, its frequency spectrum exceeds 50 MHz; the cable attenuation can therefore be expected to have a significant effect on the pulse. To quantify this, let us consider three different approaches.
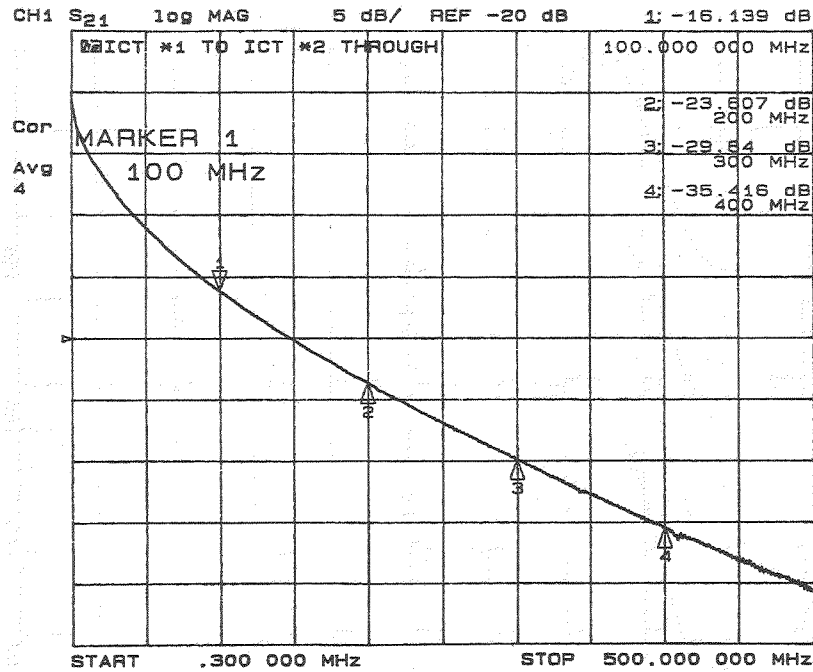
Figure 8.8. Measured attenuation of the 2 ICT cables in series.

Power Measurement If we measure the power, that is to say the energy in the signal pulse, the effect of the cable is to reduce the power by a factor F_U. If $V_1(t)$ is the voltage as a function of time for the pulse emerging from the ICT and $V_2(t)$ is the voltage of the pulse after travelling through the cable, then

$$F_U = \frac{\int\limits_{-\infty}^{+\infty} [V_2(t)]^2 \, dt}{\int\limits_{-\infty}^{+\infty} [V_1(t)]^2 \, dt} \tag{8.1}$$

Using the Parseval Theorem and the definition of S_{21}, we obtain

$$F_U = \frac{\int\limits_{-\infty}^{+\infty} |S_{21}(\omega)|^2 |V_1(\omega)|^2 \, d\omega}{\int\limits_{-\infty}^{+\infty} |V_1(\omega)|^2 \, d\omega} \tag{8.2}$$

46

Peak Measurement If we measure the peak voltage of the ICT signal pulse, the effect of the cable is to reduce the power by a factor F_P. If t_1 and t_2 are the times corresponding to the peaks in $V_1(t)$ and $V_2(t)$, respectively, then

$$F_P = \frac{V_2(t_2)}{V_1(t_1)} \qquad (8.3)$$

Expressing $V_1(t)$ and $V_2(t)$ in terms of their Fourier transforms, and using the definition of S_{21}, we can write

$$F_P = \frac{\int_{-\infty}^{+\infty} S_{21}(\omega) V_1(\omega) e^{i\omega t_2} d\omega}{\int_{-\infty}^{+\infty} V_1(\omega) e^{i\omega t_1} d\omega} \qquad (8.4)$$

Area Measurement If we measure the area of the ICT signal pulse, the effect of the cable is to reduce the area by a factor F_a, with

$$F_a = \frac{\int_{-\infty}^{+\infty} V_2(t) dt}{\int_{-\infty}^{+\infty} V_1(t) dt} \qquad (8.5)$$

Expressing $V_1(t)$ and $V_2(t)$ in terms of their Fourier transforms, using the definition of S_{21}, and using

$$\int_{-\infty}^{+\infty} e^{i\omega t} dt = 2\pi \delta(\omega) \qquad (8.6)$$

we obtain

$$F_a = S_{21}(0) \qquad (8.7)$$

47

Interpretation   We see that we can expect the energy per pulse and the peak to decrease significantly as the signal pulse travels through the cable. The area of the pulse, on the other hand, is predicted to be invariant if the cable attenuation goes to 0 (*i.e.* $S_{21} \rightarrow 1$) in the limit of $\omega \rightarrow 0$ (as can be seen in Figure 8.8, this is approximately true in the S_{21} measurement; S_{21} is near 0 dB at low frequency). The notion that the area is affected only by the transmission of the cable at $\omega = 0$ may seem counter-intuitive. It actually makes sense, however---by taking the area of the signal, we are taking its average value, and the average value of a signal is always zero, except for the part for which $\omega = 0$.

Time Domain

The effect of an RG58 cable on an ICT signal pulse produced via the pulse generator was checked with a cable that was different from the cables used for the photo-current measurements. The measurement consisted of comparing the ICT signal pulse going through the long cable to the ICT pulse going through a short cable (8 ns). The delay of the long cable was measured to be about 400 ns, making it almost twice as long as the original cables. The attenuation as a function of frequency was also measured, and found to be slightly larger than that of the 2 original cables in series. Moreover, the DC resistance of the inner conductor was measured and found to be 3 Ω; using a simple model for the DC behaviour, this corresponds to $S_{21}(0) = 0.971$. We can therefore expect $S_{21}(0)$ to be in excess of 0.98 for the original cables used for the photo-current measurements.

The signals from the long and short cables are compared in Figure 8.9. The long cable has the effect of decreasing the peak and stretching out the length. The long cable also eliminates the slight under-shoot at the end of the ICT signal. Measurements were done for a number of different drive pulse lengths; the ratio of areas and peaks are shown in Figure 8.10. Consistent with the frequency domain analysis, the peak decreases by almost a factor of 2 as the signal travels through the cable. Also consistent with the frequency domain analysis and Equation (8.7), the area is almost unaffected. Figure 8.10 has enough noise to be consistent with both an ideal case of $S_{21}(0) = 1$ and the measured value of $S_{21}(0) = 0.971$. Thus, if we take the area of the ICT signal, we hardly need to correct for the cable attenuation. If we take the peak or the energy per pulse, on the other hand, the cable matters.

The duration of the Faraday cup signal is shorter than that of the ICT (as can be seen in Figure 7.4). To check the effect of the cable attenuation on a shorter pulse, the above measurement was repeated with the drive pulse travelling directly through a long or short cable, without the involvement of the ICT. The FWHM of the pulse was about

```
5-Dec-98
20:20:40
 D:Average(3)
  .1 µs
  4.00mV

  1000 swps

 C:Average(3)
  .1 µs
  4.00mV

  1000 swps

 B:Average(2)
  .1 µs
  0.50 V

  1000 swps

 .1 µs

1 disabled
2 .2  V  50Ω
3  2 mV  50Ω        Ext  DC  -410mV  1MΩ
4 disabled
```

D

C

B

2 GS/s

☐   NORMAL

Figure 8.9. Scope traces for the through pulse (bottom), the ICT signal pulse after going through the short cable (middle), and the ICT signal pulse after going through the long cable (top).

2 ns (the shortest that could be produced by the pulse generator). As expected, the long cable produced a significant reduction in the peak voltage and a significant increase in the pulse length. The measured ratio of areas between pulses transmitted through the long and short cables was 0.984, which is consistent with the ICT results (Figure 8.10). The measured ratio of peaks was 0.177, which is significantly smaller than for the ICT signal pulse. Again, the results are consistent with the frequency domain analysis, which suggests that we can use the area of the pulse with little error due to the cable attenuation.
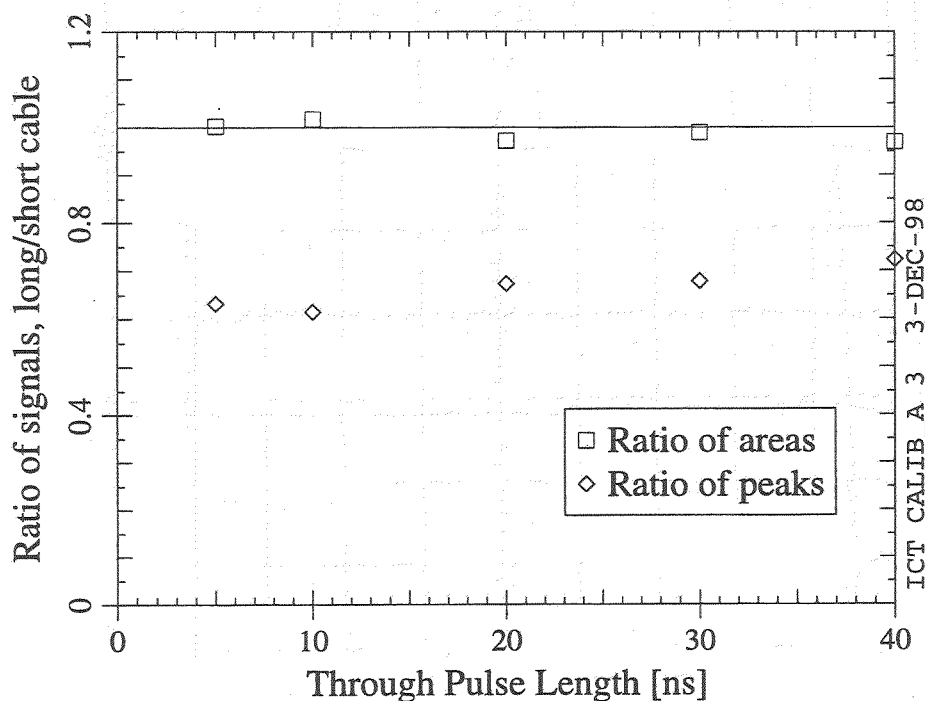
Figure 8.10. Measured effect of the long cable on the area and peak of the ICT signal.

Consistency between Different Toroids

Although detailed pulser measurements were done only on one ICT (serial number 291, not yet used for photo-current measurements), some quick pulser measurements were done on other ICT's to check for consistency. The measurements on ICT1 (serial number 242) and ICT2 (serial number 219) are summarised in Table 8.1. The ICT's were already installed on the beam line, so alligator clip transitions were used. In the first round of measurements, the background areas were not subtracted, although the Y_γ values are within ~10% of the theoretical value of $Y_\gamma = 0.8 \ \Omega^{-1}$. A second round of measurements was done with background subtraction, albeit after the connector on ICT1 had been broken off. With background subtraction, the Y_γ values for ICT2 are within 2% of the theoretical value. Since there is probably some error in the alligator clip measurement, it seems reasonable to use the theoretical value of Y_γ for ICT1 and ICT2.

50

Table 8.1. Pulser measurements on ICT1 and ICT2.

| Serial Number | Measured Y_γ [Ω^{-1}] | | | |
| | without background subtraction | | with background subtraction | |
	direct pulse	through pulse	direct pulse	through pulse
242		0.751		
219		0.703		
219	0.364	0.365	0.816	0.817

Table 8.2. Manufacturer's calibration data for three of the ICT's. The values of Y_γ were obtained by dividing the manufacturer's Q_{in}/Q_{out} values by 50 Ω.

| Serial Number | Calibration Date | Y_γ [Ω^{-1}] | | Droop [% per μs] |
		Time domain	Frequency domain	
219	Jul 1995		0.8014	3.87
242	Feb 1996	0.7941	0.7932	1.22
291	Sep 1997	0.8013	0.7979	2.88

As can be seen in Table 8.1, the results without background subtraction can be significantly off. With the pulser measurements, the base level of the drive pulse is an additional source of background. It is difficult to adjust the offset in the pulse generator to make the base level close enough to zero to have no effect on the area. So it is important to account for the background area in pulser measurements.

For comparison, the manufacturer's calibration results [8] for the 3 ICT's of interest are given in Table 8.2. As can be seen, the values of Y_γ measured by the manufacturer are all within 1% of the theoretical value of $Y_\gamma = 0.8 \ \Omega^{-1}$.

8.2. Measurement of the Dark Current

The dark current depends on the electric field in the RF gun, so it has the temporal structure of the RF pulse. The RF pulse duration is nominally 800 μs, *i.e.* of much longer duration than the photo-current bunch.[3] The ICT's are not designed to

---

[3] In principle, we expect that the dark current is modulated at the RF frequency, since field emission from a site on the surface of the gun occurs only during the half of the RF period. However, because of the ICT's slow rise time (~20 ns) compared to the RF period (0.77 ns), we do not expect to see this modulation on the ICT.

measure pulse lengths in excess of 1 or 2 μs, and their droop becomes significant for pulses longer than that. Thus, the dark current measurement with the ICT's is not rigorous. Nevertheless, semi-quantitative information about the dark current can be gleaned from the ICT's. Additional measurements were done with the pulse generator to check the behaviour of the ICT's with long pulses.

Measurements with Pulse Generator

A drive pulse of duration of 100 μs was used to simulate the dark current pulse. The ICT signal pulses produced with 2 different rise times of the drive pulse are shown in Figure 8.11. As can be seen, the ICT signal has drooped almost to zero by the end of the drive pulse; the trailing edge of the drive pulse produces a downward step in the ICT signal, which then droops to zero again. The rate of rise of the drive pulse affects the shape of the signal pulse. Since the $1/e$ decay time for the field in the RF gun is about 2.4 μs, the effect of the rise time and fall time of the drive pulse on the ICT signal is of concern.

To quantify the afore-mentioned effect, the ICT signal was measured for different rise and fall times of the drive pulse. In the actual dark current measurements, the upward or downward peak in the ICT signal transient at the start or end of the dark current pulse was recorded, so these were the quantities measured with the pulse generator. The results are shown in Figure 8.12. The ratio of the peak in the ICT signal to the current of the drive pulse is approximately constant for rise or fall times up to about 2 μs, and is about 1.16 V/A; for longer rise μs fall times, the peak starts to fall off due to the droop in the ICT. This is consistent with the manufacturer's specifications.

This brings up the following question: what are the actual rise and fall times of the dark current pulse? Although we generally expect the dark current to follow the RF electric field level in the gun, the dark current rise and fall times can indeed be somewhat shorter, since the field emission current increases non-linearly with the electric field. Taking equal rise and fall times to be a worst-case scenario, we expect the times to be about 6 μs (the time required for the RF field to fall to 10% of its initial level). Unfortunately, neither the rise time nor the fall time in the dark current ICT signal was measured. However, the dark current as a function of time was measured with the OTR screen and intensified camera, as discussed in § 5.1. According to Figure 5.2, the dark current rise time is of order 10 μs and the fall time is of order 2 μs. The fall time is plausible, but the rise time is longer than we would expect, possibly due to a

(a)

5-Dec-98
20:38:07

C:Average(3)
20 µs
50mV
—1000 swps

B:Average(2)
20 µs
4.00 V
—1000 swps

A:Average(2)
20 µs
4.00 V
—1000 swps

20 µs

1 disabled
2 1 V 50Ω
3 50 mV 50Ω
4 disabled

Ext DC -410mV 1MΩ

50 MS/s

NORMAL

(b)

5-Dec-98
20:45:52

C:Average(3)
20 µs
50mV
—1000 swps

B:Average(2)
20 µs
4.00 V
—1000 swps

A:Average(2)
20 µs
4.00 V
—1000 swps

20 µs

1 disabled
2 1 V 50Ω
3 50 mV 50Ω
4 disabled

Ext DC -410mV 1MΩ

50 MS/s

NORMAL
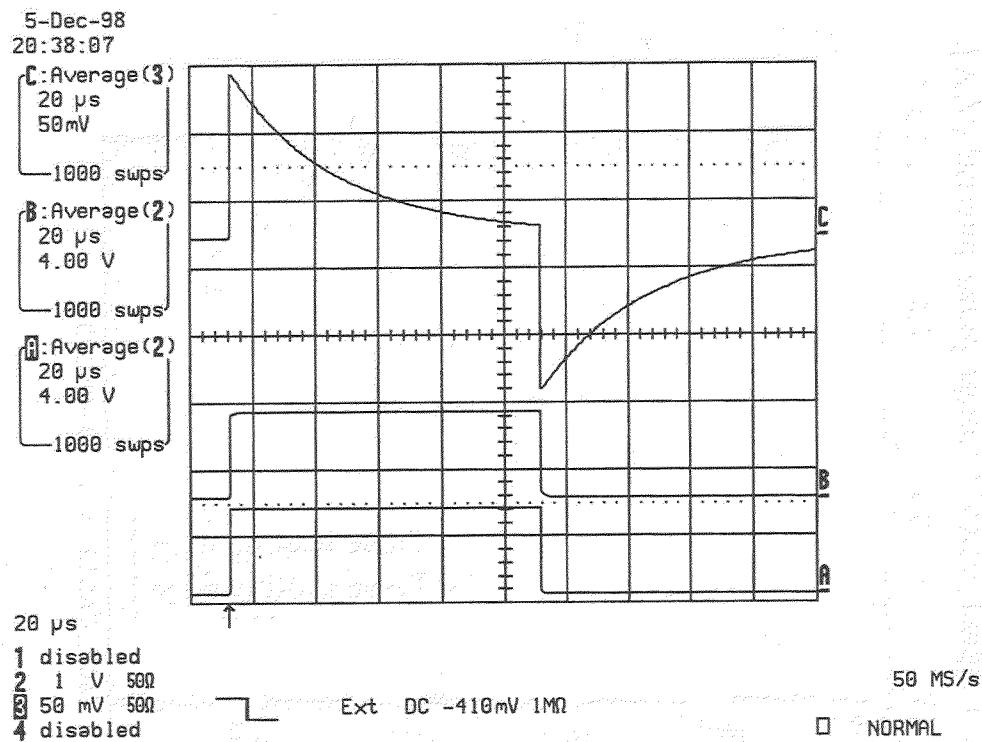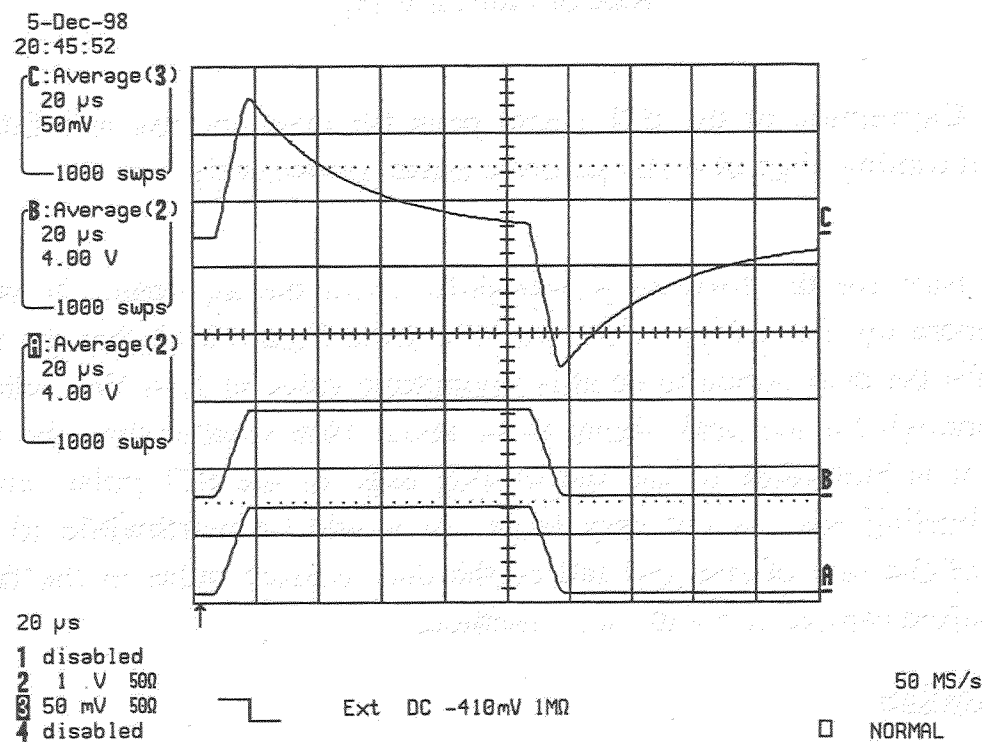
Figure 8.11. Scope traces for the direct pulse (bottom), through pulse (middle), and ICT signal pulse (top), for the case of a 100 µs drive pulse with (a) 5 ns rise and fall times and (b) 10 µs rise and fall times.
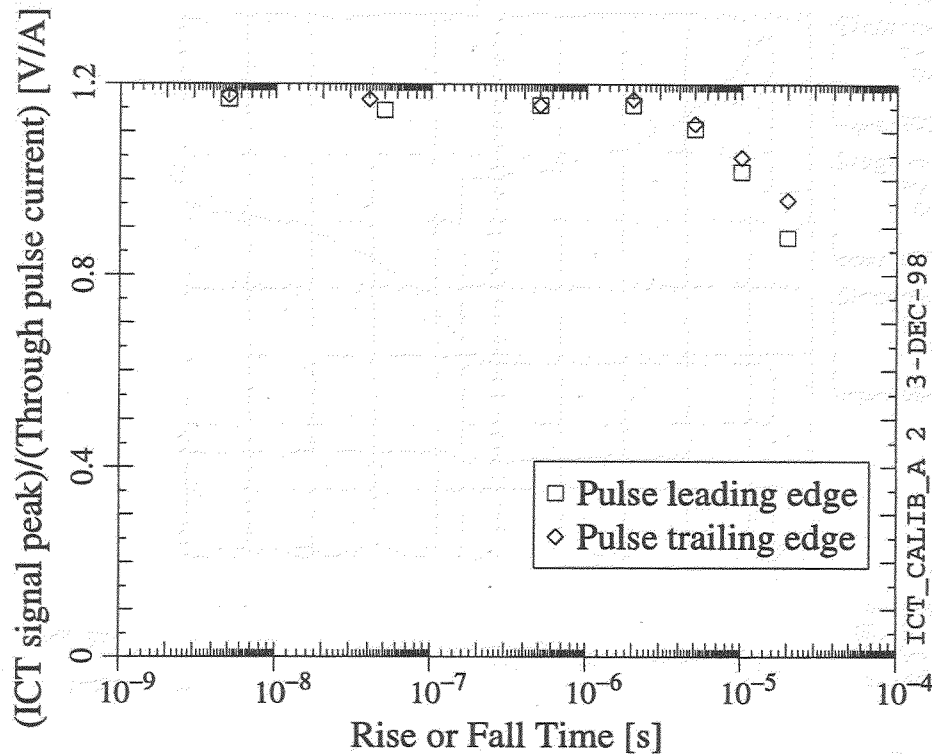
Figure 8.12. Calibration of the ICT signal peak for different rise and fall times for the leading and trailing edge of a 100 μs drive pulse, respectively.

non-zero rise time for the forward power pulse from the klystron. If we take the intensified camera results at face value, we infer from Figure 8.12 that the fall time is short enough for the peak signal to be at is asymptotic value of 1.16 V/A, while the rise time is long enough for the peak signal to be about 10% smaller than the asymptotic value. Thus, it is preferable to use the trailing edge of the ICT pulse, although the error for the leading edge is not very large. It would be worthwhile to repeat the measurement of the rate of rise and fall of the dark current pulse in the future, both with the intensified camera and with other methods.

Cable Attenuation

We saw in § 8.1 that the cable attenuation affects the height of the ICT signal peak in the photo-current measurement. Since we relied on the peak in the ICT signal for the dark current measurement, the effect of the long cable on this measurement is of concern. To check the effect of the cable, the ICT signal was again sent through the
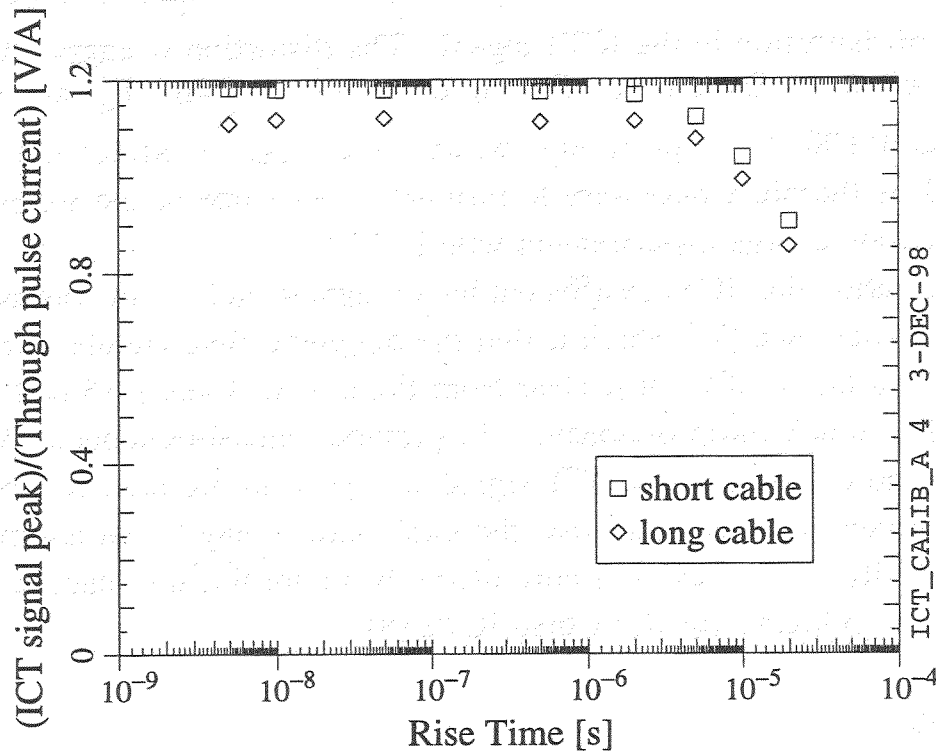
Figure 8.13. Effect of a long cable on the ICT signal peak for a 100 µs drive pulse.

long RG58 cable. Results for different drive pulse rise times are shown in Figure 8.13. The long cable produces a reduction in the peak. The reduction remains between 4 and 6% for the entire range of rise times (4 ns to 20 µs). Since this long cable has about twice the attenuation of the RG58 cables used for the dark current measurements, we can expect the effect of the original cables to be about 2 to 3%.

8.3. *ICT Saturation*

ICT1 is within the sphere of influence of the solenoids used to focus the beam in the RF gun. It was seen that the magnetic field of the secondary solenoid (the solenoid closest to ICT1) had an effect on the signal of ICT1. To quantify this effect, the pulse generator scheme (Figure 8.2) was used to measure the effect of the solenoid fields on the signal pulse from ICT1. A 40 ns pulse from the generator was passed through ICT1 for different combinations of currents in the primary and secondary solenoids. Figures 8.14 and 8.15 show the ICT1 signal for the various combinations. As can be seen, the signal is greatly reduced and distorted when the current in the secondary solenoid (I_{sec})

exceeds about 200 A. A current in the primary solenoid (I_{pri}) of about 400 A also produces a lot of distortion in the ICT1 signal. The distortion is aggravated by having both solenoids on at the same time. During operation, I_{pri} and I_{sec} are nominally of order 300 A and 100 A, respectively, which is enough to affect the ICT1 signal significantly. It is therefore necessary to turn off at least one of the solenoids in order to obtain an accurate charge measurement with ICT1.[4]

The observation that ICT1 is affected by a magnetostatic field contradicts the ICT manufacturer's experience [7], which is that the magnetic field should at most increase the droop rate by a factor of 2. It is clear from Figures 8.14 and 8.15 that the observed effect for ICT1 is much more dramatic. In previous measurements at Argonne with ICT2, however, no decrease in the ICT signal was seen in the presence of a magnetic field. The manufacturer speculates that the explanation may be an anomalously high relative permeability on the read-out core of the ICT1 toroid; the relative permeability is about a factor of 3 higher for ICT1 than ICT2 [8].

8.4. Summary

Pulser measurements on the ICT's allow us to draw the following conclusions for the measurement of photo-current:

1. The area of the ICT signal pulse should be used. It is important to subtract the background area.

2. It is acceptable to use the theoretical relationship, *i.e.* Equation (7.4) to calculate the charge from the area of the signal pulse.

3. As long as the area is used, the correction for the cable attenuation is small (1 to 2%).

Likewise, for the measurement of dark current, we conclude that

1. The peak in the ICT signal at the beginning or end of the RF pulse may be used when the RF gun field fills and decays normally; there may be some advantage to using the end of the RF pulse.

---

[4] In the future, ICT1 will not be as close to the gun, so the influence of the solenoids on the ICT1 signal may be lessened.

(a)
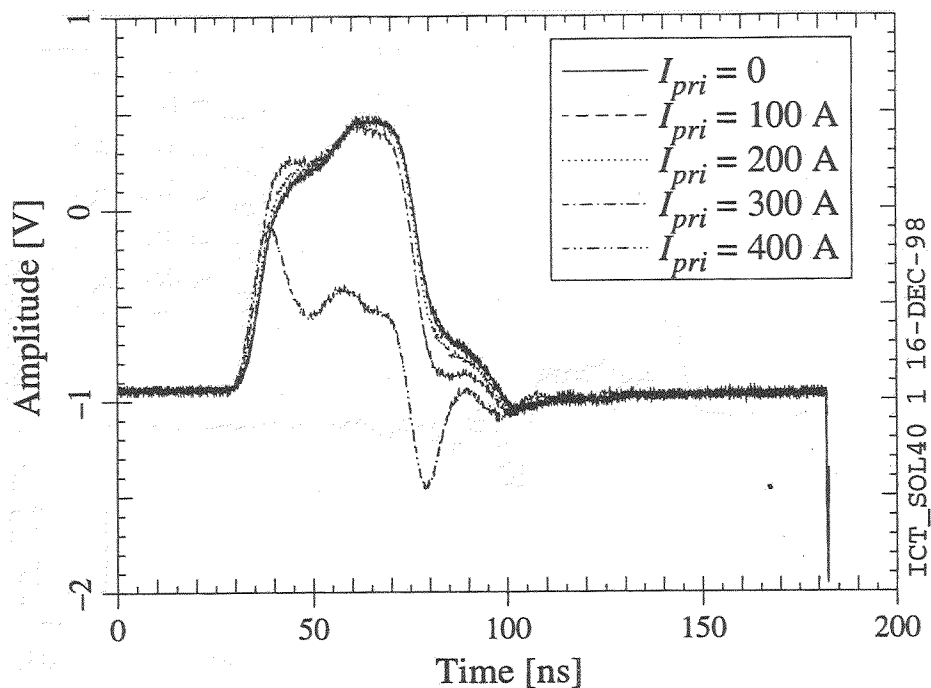
(b)
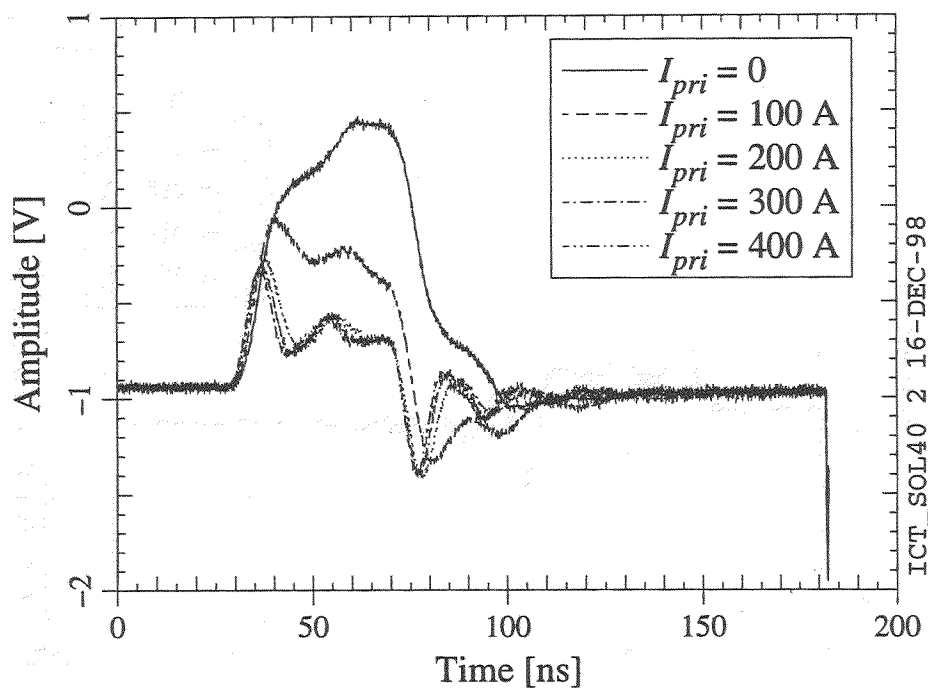
Figure 8.14. Comparison of the ICT1 signals produced by a 40 ns pulse with different values of I_{pri}, for (a) $I_{sec} = 0$ and (b) $I_{sec} = 100$ A.
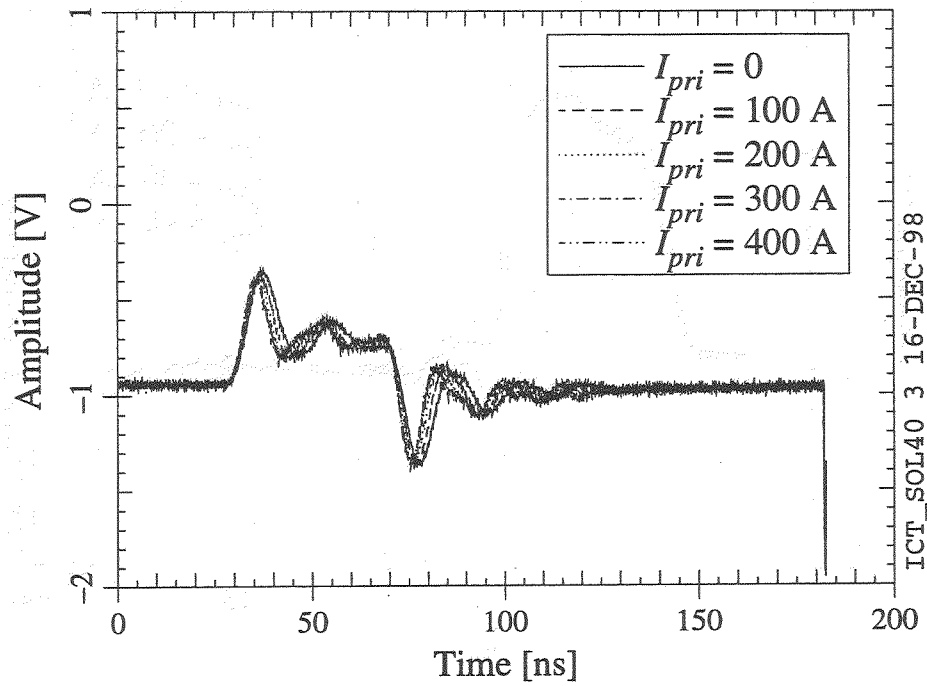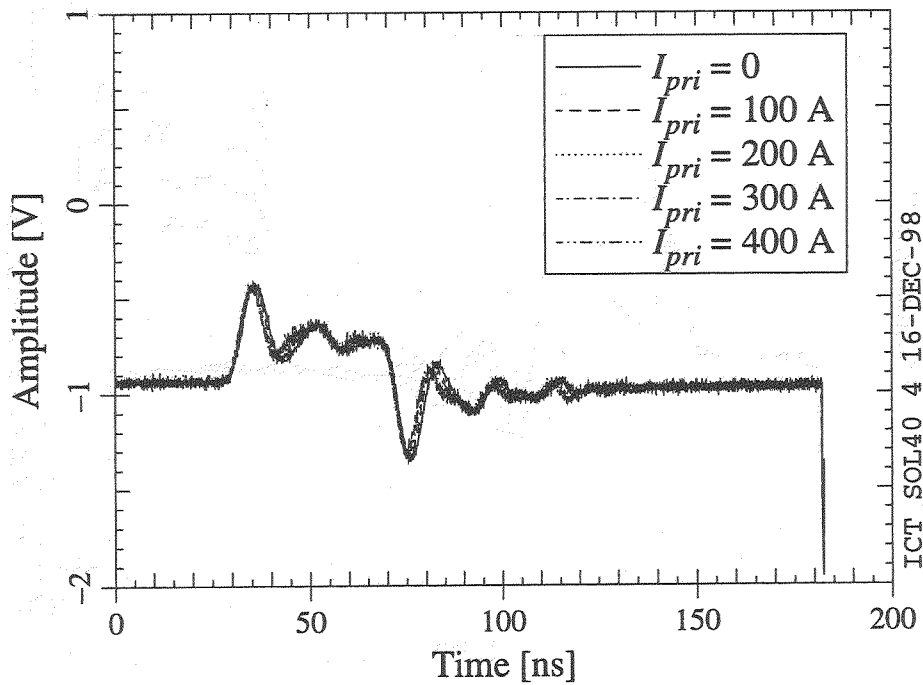
Figure 8.15. Comparison of the ICT1 signals produced by a 40 ns pulse with different values of I_{pri}, for (a) $I_{sec} = 200$ A and (b) $I_{sec} = 300$ A.

2. For a normal fill or decay, the dark current I can be calculated approximately from the peak V_P in the ICT signal via

$$|I| = Y_d |V_P| \qquad (8.8)$$

with

$$Y_P \approx \frac{1}{1.16\,\Omega} = 0.86\,\Omega^{-1} \qquad (8.9)$$

3. For a normal fill or decay, the droop should produce at most a 10% error, depending on the actual rise or fall time of the dark current.

4. For a normal fill or decay, the correction for the cable attenuation should be at most 2 or 3%.

5. In the case of a slow fill (due to shaping the forward power pulse for the gun or in the case of the superconducting cavity), the ICT signal will depend not only on the current, but also on the fill rate.

6. It would be good to remeasure the rate of rise and fall in the dark current signal.

For both types of measurements, the ICT1 signal is compromised if the solenoids are at their nominal settings.

9.1. BPM system overview

The BPM is a button style pickup, with buttons which are 1 cm in diameter located 3 cm radially from the center of the beam pipe. Each detector has four buttons, a top and bottom pair for the vertical position measurement, and a left and right pair for the horizontal position measurement. Without any extra front end processing, the raw signal from each button goes into a bandpass filter centered on 53 MHz, followed by log amplifiers. The difference Log(button1)-Log(button2) is then held for sampling. The purpose of some of the BPM studies has been to investigate additional processing of the raw signals before they go into 53 MHz filters.

9.2. Initial studies on basic functionality

The purpose of the first study was to verify the existence of a usable position signal. It was possible to examine the sum and difference signal from a pair of buttons. The sum signal, which should be proportional to beam intensity, was found to be linear with the peak to peak voltage as seen on ICT1. The difference signal, which should be proportional to beam position, and the sum signal were found to be independent. The sum signal (beam position) was found to vary linearly with the current setting on the upstream steering coil.

9.3. Studies on upstream signal processing

Three hardware arrangements were compared:

1. Original Ed Barsotti bandpass filter and log amplifier configuration.
2. Output of the button to a bandpass filter, followed by a mixer to bring the signal down to 53 MHz before transport from the cave, followed by the original Barsotti configuration.
3. Output of the button directly to the 53 MHz mixer, and then out of the cave to the original Barsotti electronics.

It was found that the signal was maximized when (approximately) 1.6 GHz was mixed down to 53 MHz. In other words, the response of the capacitive button pickups is greatest around 1.6 GHz. The signal arriving at the processing electronics was

largest with the mixer present, but without the bandpass filter, the insertion loss from the filter being fairly large.

It was observed that there was significant modulation of the raw BPM signal at 1.3 GHz. A notch filter was put in which successfully removed this modulation.

10/ RF GUN PROPERTIES

We measured the resonant frequency, the cell-to cell coupling, and the passband width of the RF Gun. The measurements were made on 1/30/98, one month after the end of the experiments with the beam.

A Network analyzer (NWA) measurement of the gun TM_{010} passband is shown in Figure 10.1.

A summary of the properties of the accelerating passband is given in Table 10.1. We did not measure the temperature of the gun but we estimate that it was around $25°C$. The pressure in the gun was 3.9×10^{-11} Torr according to the ionization gauge.

Table 10.1. RF Gun properties

Parameter	Unit	Simulation	Measurement
pi-mode frequency	MHz	1300	1299.5055
0-mode frequency	MHz	1297.154	1296.939
Coupling	%	0.2	0.2

The measured π-mode frequency is 495 kHz lower than expected. To explain the difference, we thought first about the temperature of the gun.

Influence of the temperature on the gun frequency

The frequency of the T_{010} mode for an ideal pill-box cavity is given by the relation (ref 9, p.110) :

$$f_{010} = \frac{p_{01} \times c}{2\pi R}$$

with :
- $p_{01} = 2.405$
- $c = 3 \times 10^8 \ ms^{-1}$
- R = radius of the pill-box

Because of thermal expansion, the temperature changes the radius of the cavity, and hence the frequency. An increase of the temperature of the gun will decrease the resonant frequency :

$$\frac{df_{010,\pi}}{dT} = -\frac{p_{01}}{2\pi} \frac{c}{R^2} \frac{dR}{dT} = -\frac{p_{01}}{2\pi} \frac{c}{R^2} R_0 \alpha \approx -\frac{p_{01}}{2\pi} \frac{c}{R} \alpha$$

with :
- $R = R_o[1 + \alpha(T - T_0)]$
- α = thermal expansion coefficient of copper
- R_o = radius of the pill-box at temperature T_0.

<u>For the AO photoinjector:</u>
- $R = 8.83 \times 10^{-2} \ m$
- $\alpha_{copper} = 16.8 \times 10^{-6} \ mm/mm \ °C$ at ambient temperature

This gives:

$$\left(\frac{df_{010,\pi}}{dT}\right)_{Gun} \cong -22 \ kHz/°C$$

A decrease in frequency of 495 kHz corresponds to an increase in cavity temperature of about 23 °C. Such an increase in temperature is too large to explain the low measured frequency of the π-mode .

We thought also that an incorrect placement of the photo-cathode could explain this shift of frequency. Indeed, the photo-cathode we used had been placed in the gun in the beginning of October and we didn't check whether if the gun was tuned. Unfortunately, the cathode had been removed from the gun by the time we analyzed our results.
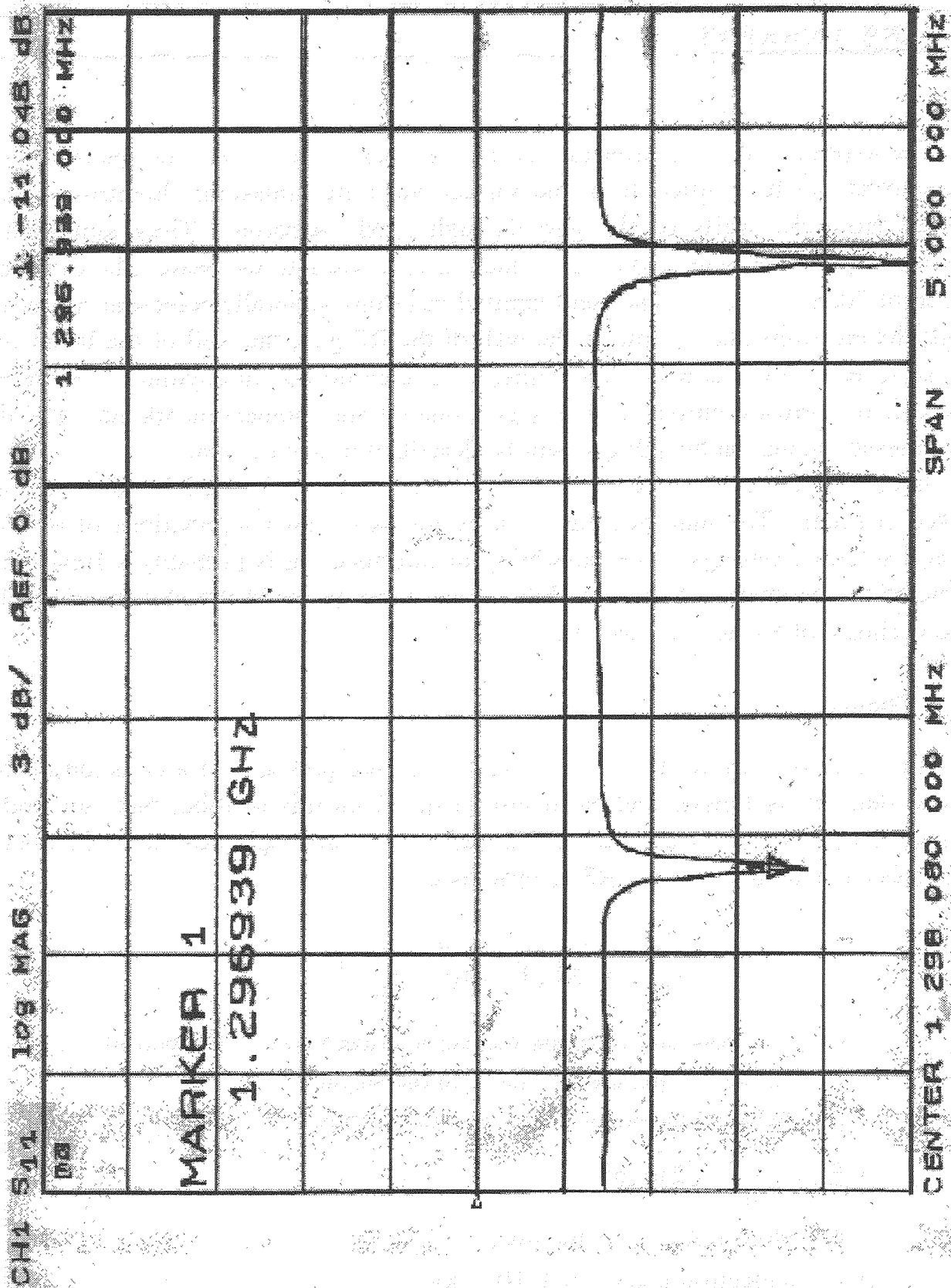
Figure 10.1. S_{11} measurement of the fundamental passband of the RF gun.

The exposure of a material to a surface electric field lowers the energy barrier and electrons can be emitted from the surface via field emission. Electrons can be extracted from the walls of the gun through field emission. They can then be accelerated by the RF field, and some of them may travel into the beam tube to become a source of "dark current". The field emitted electrons generally represent a nuisance current; the electrons end up hitting the wall of the RF gun, the wall of the beam tube, or the surfaces of other downstream elements. If they do not hit anything, they remain a source of background current with a large temporal and momentum spread. The dark current measurements on the RF gun will be described in this section.

Signs of multipacting in the gun during the fill or decay in the RF pulse were also observed at times. The multipacting occurred for particular combinations of RF field level and solenoid settings. The possibility of multipacting is probably a flaw that is intrinsic to the geometry of the gun, but we can hope to avoid the multipacting via a judicious choice of RF and solenoid fields.

11.1.   Theory

The emission current density for a surface in the presence of a constant electric field was derived by Fowler and Nordheim [10]. From this relation, one can find an approximate expression for the current emitted by a microscopic protrusion located on a metal surface in an *alternating* RF electric field:

$$\langle I_{FN} \rangle \propto \left(\beta E_s \right)^{2.5} \exp\left(-\frac{E_0}{\beta E_s} \right) \tag{11.1}$$

where
- $\langle I_{FN} \rangle$ = Fowler-Nordheim current averaged over 1 RF period
- E_s = macroscopic electric field on the surface
- β = field enhancement factor due to protrusion
- $E_0 = \dfrac{8\pi}{3hq_e} \sqrt{2m_e \phi^3}$
- ϕ = work function of the metal
- m_e = electron mass = $9.1 \cdot 10^{-31}$ kg
- q_e = electron charge magnitude = $1.6 \cdot 10^{-19}$ C
- h = Planck constant = $6.62 \cdot 10^{-34}$ J.s

In this model of enhanced field emission, the electric field is magnified locally by imperfections in the metal surface, and the field emission current is produced preferentially at the site of the microscopic imperfections. The imperfections may be microscopic whiskers or particles stuck to the surface. The β factor is the ratio of the microscopic electric field near the imperfection to the macroscopic electric field in that part of the wall of the RF gun.

According to Equation (11.1), we should obtain a straight line by plotting $\ln\left(\dfrac{\langle I_{FN}\rangle}{E_s^{2.5}}\right)$ as a function of E_0 / E_s, and the slope of the line should be equal to $-1/\beta$. This is the "Fowler-Nordheim" plot which allows us to determine the field enhancement factor.

11.2. Experiment

The dark current produced by the RF gun as a function of field level was measured periodically to see whether there was any decrease due to conditioning. The value of the field enhancement factor β was also estimated.

Field Level Measurement

The field level in the gun was varied by adjusting the forward power supplied by the klystron. The field level was inferred from the forward power as follows:

1. The peak forward power in the RF pulse was measured using a diode to sample the signal of a waveguide directional coupler at the exit of the klystron. The actual forward power was obtained via a calibration formula for the diode and a coupling factor for the directional coupler.

2. The transmission through the circulator between the exit of the klystron and the gun was measured in order to deduce the forward power that reaches the gun. The measured power transmission factor with a matched termination of the waveguide was 82.5%. Assuming unity input coupling, the forward power that reaches the gun is equal to the dissipated power in the gun.

3. SUPERFISH [11] was used to obtain a theoretical value for the surface field distribution and power dissipation in the RF gun for a given stored energy. According to SUPERFISH, the power dissipation is 2.16 MW when the field at

the cathode $E_{cathode}$ is 35 MV/m. We assume the Q of the gun is independent of field level, so that the power dissipation is proportional to $E^2_{cathode}$. Thus, we can calculate the field at the cathode from the forward power signal of the diode. We calculate the peak value of the field at the cathode, not the RMS value.

Current Measurement

We measured the dark current with ICT1, which is immediately downstream of the gun. We turned off the solenoids in order to avoid distortion in the ICT1 signal. We used Equation (8.8) to obtain the current from the peak to peak in the transient of the ICT signal at the beginning or end of the RF pulse (usually the latter). As discussed in § 8.2, we expect an error of at most 12 or 13% due to the slow rise or fall of the dark current pulse and the cable attenuation. The current measured with the ICT is an average current in the sense that it is average over the RF period; it is a peak current in the sense that it is not multiplied by the duty cycle of the RF pulse train.

Results

Extensive RF processing of the gun was done with a molybdenum cathode. A Mo cathode of nominal diameter was used initially. Later, a Mo cathode of slightly larger diameter was tried; the hope was that the reduction in the gap between the cathode and the wall of the gun would reduce the dark current. Measurements of the dark current at various times with the small- and large-diameter Mo cathodes are compared in Figure 11.1a. As can be seen, there is very little reduction in the dark current over 4 months. Moreover, the change in cathode diameter has no significant effect on the dark current. An initial round of RF conditioning was done with a copper cathode and, naturally, the gun was operated with a coated (Cs_2Te on Mo) cathode. Measurements with the different cathodes are compared in Figure 11.1b. There is not much difference between Mo, Cu, or coated Mo. On the other hand, as can be seen in Figure 11.1b, the dark current is significantly higher when the cathode is withdrawn completely.

When the dark current results were first analysed, somewhat different conversion factors were used for the both current and the field level, due to less accurate calibration and due to misunderstanding of the theoretical values from SUPERFISH. The results shown in Figure 11.1 incorporate the revised field conversion and improved calibration factors for the circulator loss (see above) and the ICT current (see § 8.2).
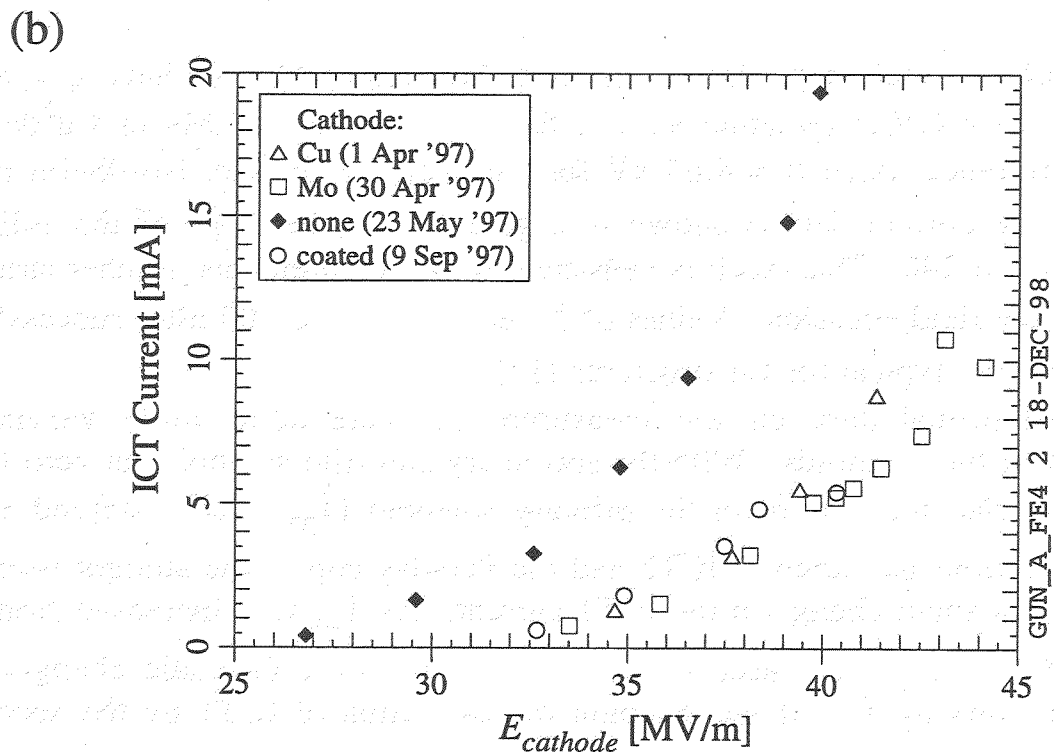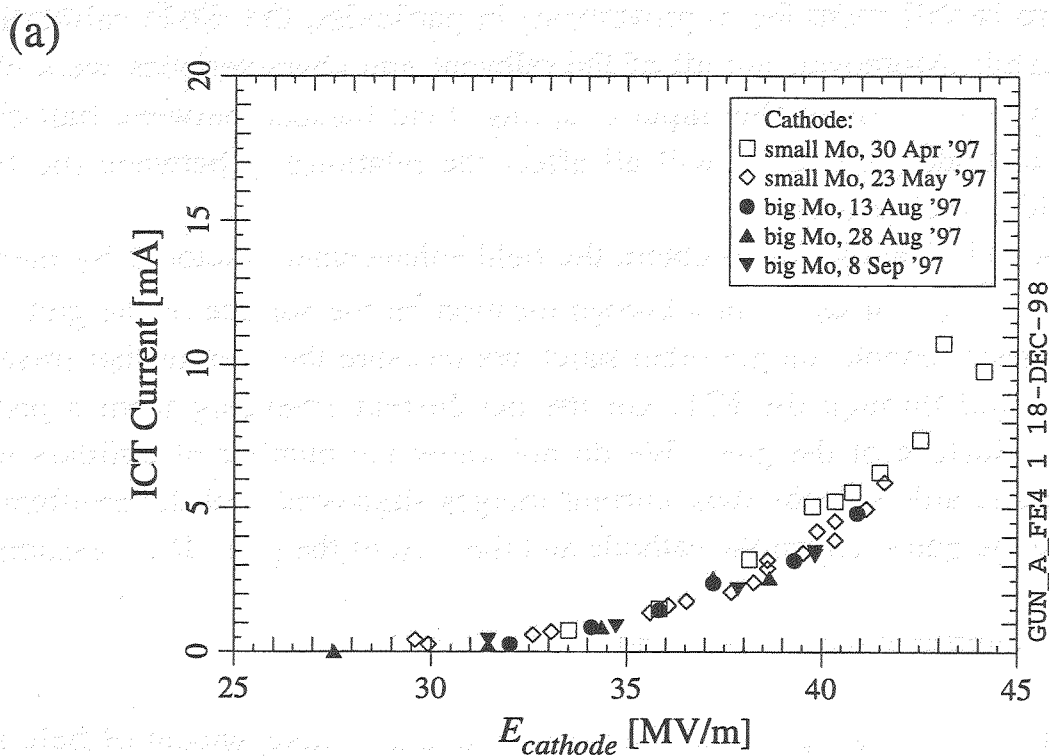
(a)

(b)

Figure 11.1. Comparison of dark current measurements (a) on Mo cathodes of different diameters and (b) on cathodes of different materials.

However, there is still room for improvement; in particular, the diode calibration has not been checked. Moreover, not all of the relevant gun characteristics were checked after the gun was retro-fitted (the input coupling, field balance between half-cell and full cell, and cathode penetration will all affect the relationship between the forward power and field at the cathode).

Equation (11.1) allows us to obtain the field enhancement factor β by measuring the net field emission current from a known location on the surface of the gun. In our dark current measurements, on the other hand, we measure the current that travels into the beam tube and through the ICT, not the net current emerging from a particular location on the surface of the gun. We do not know the number of emitters or their locations for sure, although the dark current images suggested that the emitters might be located near the gap between the cathode and the wall of the gun. If we assume

1. a single emitter at the cathode, and

2. the ICT measures a fraction of the net current that is independent of field level,

then we can infer a value of β. Using the work function of Mo, we have $\phi = 4.6$ eV [12] and $E_0 = 67.4$ GV/m (whether we use the work function of Mo or Cu does not make a big difference, since $\phi = 4.65$ eV for Cu [12]). A Fowler-Nordheim plot of some of the dark current data is shown in Figure 11.2. The slope of the solid line corresponds to $\beta = 240$. This result is consistent with measurements in other structures plagued by heavy field emission. Values of β between 50 and 100 after successful RF processing are more typical for Cu structures [13].

Some additional dark current measurements were done while varying the magnetic field of the solenoids. With the secondary and trim solenoids at zero ($I_{sec} = I_{pri} = 0$), we varied the current in the primary solenoid (I_{pri}), and observed a large change in the current measured at ICT2 and the Faraday cup in the straight beam line (FC1), but only a small change in the ICT1 current. As I_{pri} was increased from 0 to 300 A, the FC1 current decreased by a factor of 10. Less dramatic changes were observed when varying I_{sec}, if we discount the saturation of ICT1 by the secondary solenoid.
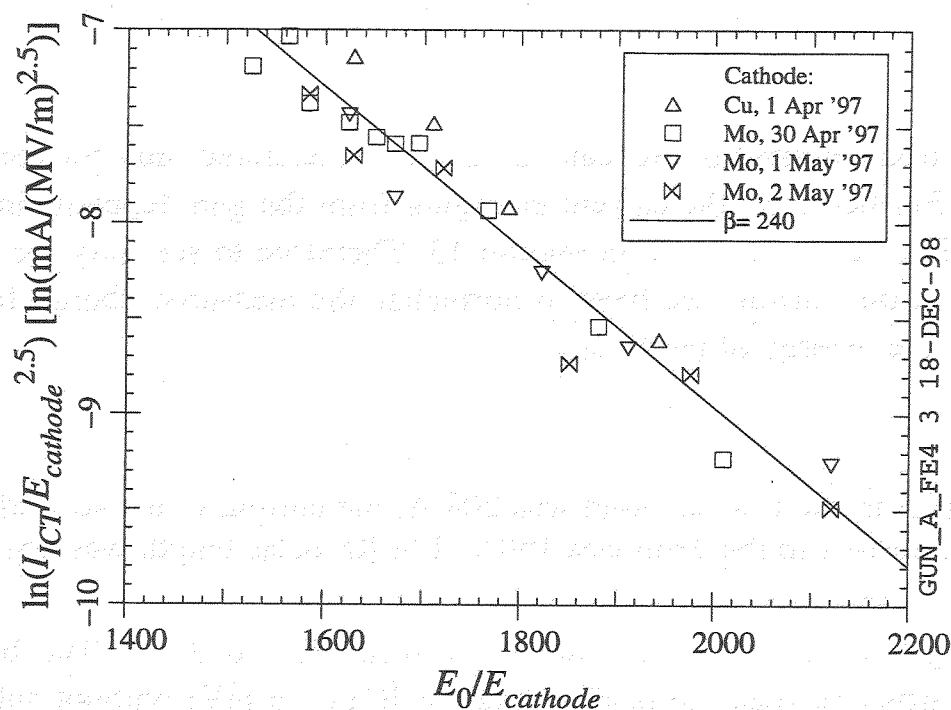
Figure 11.2. Fowler-Nordheim plot of selected dark current data.

11.3. *Summary*

Our measurements indicate that the gun produces 1 to 2 mA of dark current at the nominal field level of E_{cath} = 35 MV/m, which we might consider to be an excessively high amount of dark current. The dark current is not reduced by RF conditioning. There is evidence that suggests that the dark current is produced near the cathode; we may speculate that the retro-fit of the gun for the new type of cathode is the root cause of the problem. The geometry in the vicinity of the cathode will be different in future guns.

Principle

The electrons emitted by the cathode can be accelerated only for some values of the RF phase. Furthermore, the current emerging from the gun depends linearly on the energy of the laser as we will see in section 13. Therefore to see only the influence of the RF phase on the current, we have to normalize the measured charge from the ICT by dividing by the energy of the laser.

Experiment

The current in the first solenoid was 208 A; the current in the secondary solenoid was 198 A; the current in the Trim was 100A. The RF pulse length was 46 μs.

The RF phase was set by the Macintosh from $90°$ to $260°$. The beam current was measured using the peak-to-peak voltage of ICT1 (in mV) without subtracting the background. The energy of the laser was measured using a laser photo-diode signal (in mV) as described in section 13.

Figure 12.1 shows the ratio of ICT1 to laser photodiode signal versus relative RF phase. As expected, we see a value of the phase for which the current is a maximum, i.e the relative RF phase which accelerates the maximum number of electrons.
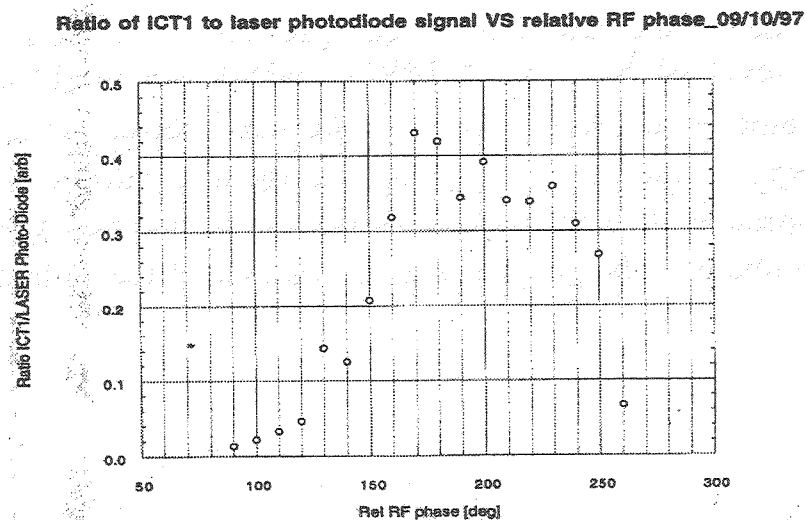
Figure 12.1. Ratio ICT1 to laser photo-diode versus relative RF phase

The A0 photoinjector uses the photocathode material cesium telluride (Cs_2Te). Cs_2Te has high quantum efficiency, relative ease of fabrication, good vacuum ruggedness, "recoverability" by heating, and a proven record in RF photoinjector use at LANL. This section summarizes quantum efficiency measurements made on two cesium telluride (Cs_2Te) photocathodes from June 1997 to December 1997. This section does not describe the photocathode preparation chamber, photocathode fabrication, or details of the measurements of the DC quantum efficiency of the photocathodes. These topics will be discussed in an internal report currently in preparation.

13.1. *Photocathodes Used in the RF Gun*

Photocathode #1 was used in the RF gun from June 1997 to July 1997 (run 1). Photocathode #2 was used in the RF gun from August 1997 to December 1997 (run 2).

13.2. *DC Quantum Efficiency Measurements*

The quantum efficiency of each Cs_2Te cathode was measured by monitoring the photocurrent off the cathode under illumination from a calibrated, continuous (DC) mercury vapor lamp. Lenses and apertures were used to project a circular spot of approximately 0.5-1.0 cm diameter onto the cathode.

The DC QE of PC1 was measured to be 13% prior to run 1. At the end of the run 1, the DC QE was measured at 0.65%. Photocathode #1 was rejuvenated by heating, and recovered to a DC QE of 10.1%, but was not used in the RF gun after that point.

Immediately after its fabrication, the DC QE of PC1 was measured to be high as 16% after extended illumination with the UV lamp. Without UV illumination, the QE dropped to a base value of about 8%.

The spatial uniformity of each photocathode was measured by focussing the UV light from the mercury lamp to a spot size of approximately 1.6 mm^2. This spot was then scanned across the surface of the photocathode, and the quantum efficiency was measured at each position. The efficiency varied from slightly higher than the maximum value near the center to <1% near the edge of the exposed substrate.

13.3. *Quantum Efficiency Experimental Setup and Diagnostics*

Overview

QE measurements were taken with illumination from a single laser pulse and with illumination from trains of up to 50 laser pulses spaced by 1 μs. Under both conditions, the quantum efficiency was based on the measurement of the charge in a *single* electron bunch; no attempt was made to quantitatively measure the charge of all electron bunches during laser pulse train illumination. Qualitative measurements, recorded from oscilloscope traces, show that the electron emission follows the laser amplitude throughout the pulse train.

Laser Energy Diagnostics

In almost all of the QE measurements, the UV energy was determined by measuring the maximum voltage of a single UV pulse measured from a photodiode in the laser room which monitored a small fraction of the laser pulse reflected from a beam splitter. The relation between the photodiode voltage and the laser energy was determined by inserting a calibrated energy meter after the beam splitter, before the mirror leading to the laser beam transport system. The photodiode voltage (single pulse) and the laser energy (entire pulse train) were measured by two oscilloscopes and captured by a computer for many shots. This gave a relation between the single-pulse photodiode voltage and the laser pulse-train energy inside the laser room. The energy in a single pulse is given by the total pulse train energy divided by the number of pulses. It must be noted that this method for determining the energy of a single pulse is accurate only if the entire pulse train has a flat energy profile during the calibration. Because there are typically 10-15% variations in the flatness of the pulse train, many data points were taken, and a statistical average was used for the final calibration constant.

In two sets of measurements, there was enough energy in a single laser pulse (rather than a train of pulses) to give a strong reading on the energy meter after the beam splitter. For these measurements, there is less uncertainty in the calibration of the photodiode response.

All of the photodiode-based calibrations had to be repeated on a regular basis. Each time the laser was realigned or adjusted, the reflected laser pulse had to be carefully aligned onto the small active area of the photodiode. In order to ensure an accurate calibration, the comparison between the photodiode and the laser energy was

repeated each time a significant change was made. A typical calibration of the photodiode is shown in Figure 13.1.

In the last two sets of QE measurements, the laser beam splitter was calibrated with a laser energy meter monitoring the reflected light from a single laser pulse, and another meter monitoring the transmitted laser light. Because the laser energy meter has a larger active area and a well known response, these measurements gave the smallest uncertainty in the laser energy calibration.

One source of uncertainty in the measurements which has not been precisely determined is the cable attenuation for the ICT and laser signals. All of the laser calibrations were taken on oscilloscopes inside the laser room with ~50 ns RG58 cable lengths between the photodiode and the oscilloscope. Some measurements were taken with the LeCroy scope located near the relay racks with the photodiode signals propagating from the laser room through an additional 87 ns of 3/4 inch Heliax cable. Although the attenuation of the photodiode signal in the Heliax has not been measured, it is not expected to be a significant effect.

The ICT signals propagated through ~242 ns long RG58 cables from the cave to the relay racks. In the case of the energy meter-based laser energy measurements, the ICT signals were sent through the same Heliax cables and approximately 32 ns of RG58. As discussed in § 8.1, however, we do not expect the cable attenuation to have a significant effect on the area of the ICT signal. Thus, a 100% cable transmission is assumed.

To determine the laser energy on the photocathode, the optical transmission of the beam transport system was measured up to the final vacuum window in the gun. In run 1, the transmission was 15%; in run 2, the mirrors in the transport system were changed, and the transmission increased to 58%.

The transmission of the final, uncoated, quartz window and the reflectivity of the dielectric mirror in vacuum were measured after the beam line was disassembled. The net transmission from the outside of the vacuum system to the cathode was found to be 80%. It is not known whether the laser beam partially clipped one of the apertures between the mirror and the cathode; to be conservative (and obtain the lowest QE estimate), we assume that it was not clipped.

Bunch Charge Diagnostics

In each QE measurement, the electron bunch charge was measured with a combination of ICT 1, ICT 2, and the Faraday flange at the end of the straight beam

line (FC1). The charge per bunch was obtained from the time-voltage area of the ICT and Faraday flange signals using Equations (7.4) and (7.3), respectively.

Because of its upstream location, ICT 1 was monitored in almost every QE measurement. However, as discussed in § 8.3, the response of ICT 1 was affected by the magnetic field generated by both the primary and secondary solenoids; the response of ICT 1 can only be trusted to be accurate when both solenoids were turned off or were at low current. ICT 2 and FC1 produced reasonable signals only when the electron beam was aligned through the entire beam line.

13.4. *Pulsed Quantum Efficiency Measurements*

Overview

The QE of PC1 was measured in two experiments during run 1, once to determine the relative QE vs. RF field, and once to determine QE vs. laser position on the photocathode. In both measurements, the electron beam and laser beam diagnostics were not accurately calibrated to give a high-confidence value for the QE.

The QE of PC2 was recorded via scope-trace print-outs several times during run 2, and seven specific experiments were done to measure photoemission as a function of RF phase, RF power, laser position on the photocathode, and to measure the relative response of the electron diagnostics. Experiment numbers are assigned based on the date on which they were performed as QE_yymmdd (yy - year, mm - month, dd - date). A summary of QE measurements is given in Table 13.1.

In experiment QE_971107, the position of the laser spot was moved in five positions on the photocathode. Figure 13.2 shows the bunch charge and QE vs. laser energy for the spot located above the center of the photocathode. A single laser pulse was used in the calibration of the photodiode and in the photocathode illumination. The variation in the QE for the five spots is given in Table 13.2.

The same measurements were repeated a few days later in QE_971110, and the data for the centered laser spot is shown in Figure 13.3. Figure 13.4 gives the histogram and statistics of the QE values for the same set of data.

In December 1997, higher laser energy was available to extract much higher bunch charge from the photocathode. The highest recorded charge extracted during this period was just over 30 nC in a single bunch and 15 nC/bunch in nine bunches. Experiment QE_971208 measured QE as a function of extracted charge. The results from one measurement are shown in Figure 13.5. The overall QE is significantly lower than in QE_971110, most likely due to degradation of the photocathode during the

Table 13.1. Description of the nine pulsed QE experiments from PC1 (970626) and PC2 (all others). The "best estimate" of the QE for each experiment is given, and represents the highest confidence measurement or an average of several measurements made during the experiment.

Experiment #	experimental goal (Q=charge)	best estimate QE value
970626	Q vs. RF power	—
	Q vs. position	
970910	Q vs. phase	—
970922	QE, ICT 1 and ICT 2	9.1%
970925	QE vs. position	—
971107	QE vs. position	6.1%
971110	QE vs. position	4.5%
971208	QE vs. position	0.5%
971212	QE vs. charge	0.5%

Table 13.2. Average QE value and standard deviation for five positions on the photocathode.

Position	average QE	standard deviation
top	3.64 %	0.32
bottom	2.98 %	0.25
left	6.11 %	0.52
right	1.25 %	0.20
center	2.96 %	0.21

preceding month. The data also show that for bunch charges higher than 5 nC, there is a significant decrease in QE due to space charge masking of the electric field. This is caused in part by the short duration of the laser pulse, which is estimated to have been $\leq$ 5 ps during these experiments. Longer laser pulses will allow the charge to be moved away from the photocathode by the RF field during the laser pulse, decreasing the space charge current limitation.

13.5. *Summary*

The QE data from Run 2 gave predictable results. The highest QE measurement was on the order of 4-5%, which is consistent with the DC QE measurements and the uncertainty in the value of the pulsed QE measurements. The QE started out high, and then decreased as the photocathode became contaminated from exposure to residual gasses in the gun. The photoemission current decreased with increasing charge as a result of the high space charge density of the bunch. Although the spatial variation of the pulsed QE was not directly compared to the variation of the DC QE, the results were qualitatively similar.

ICT 1 was strongly affected by stray magnetic fields from the primary and secondary solenoids, and because the solenoid settings were not always recorded, there is some degree of unknown error in these QE measurements. In the next set of experiments, a strong effort must be made to make sure the upstream ICT is not affected by the solenoid fields.
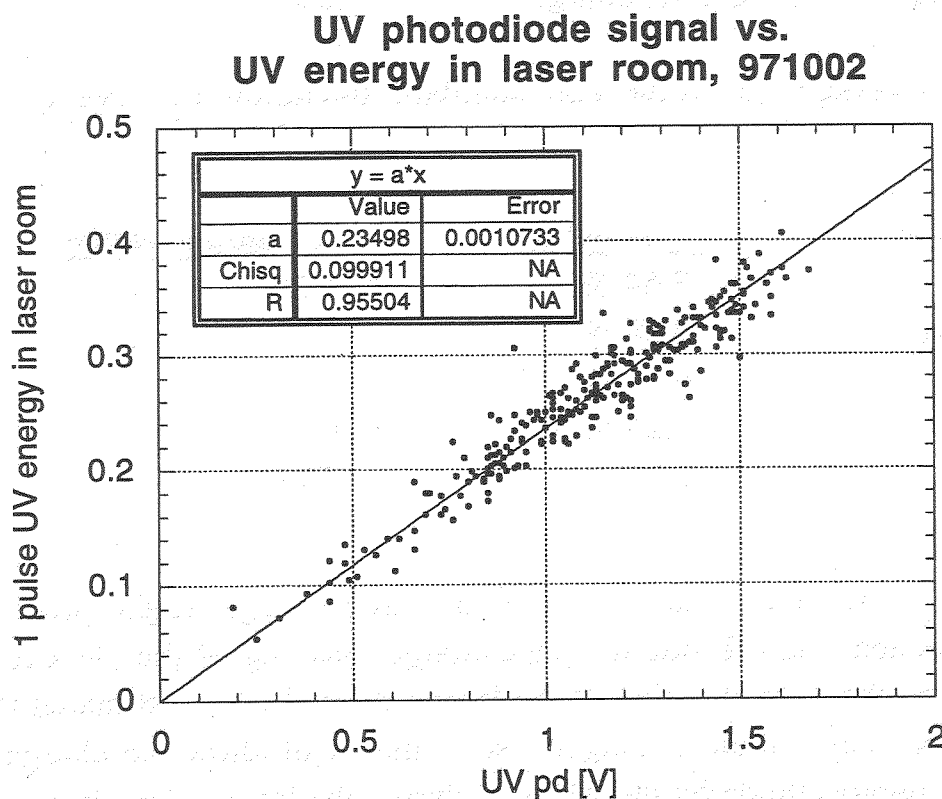
Figure 13.1. Typical calibration of the UV monitor photodiode to the UV energy in the laser room. The slope of the curve fit was used to determine the calibration constant.
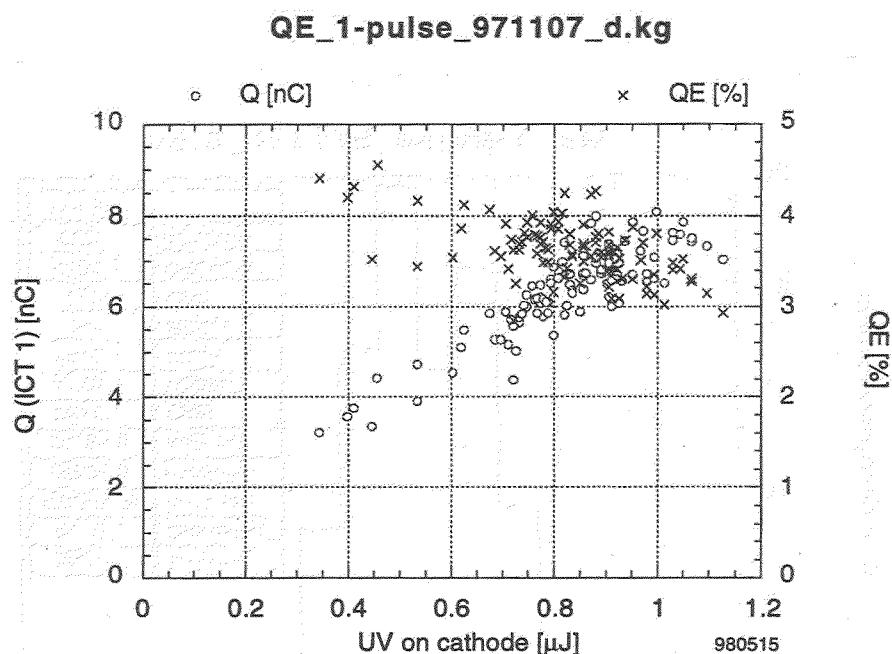
Figure 13.2. QE measurement of the Cs$_2$Te photocathode with single laser pulse illumination.
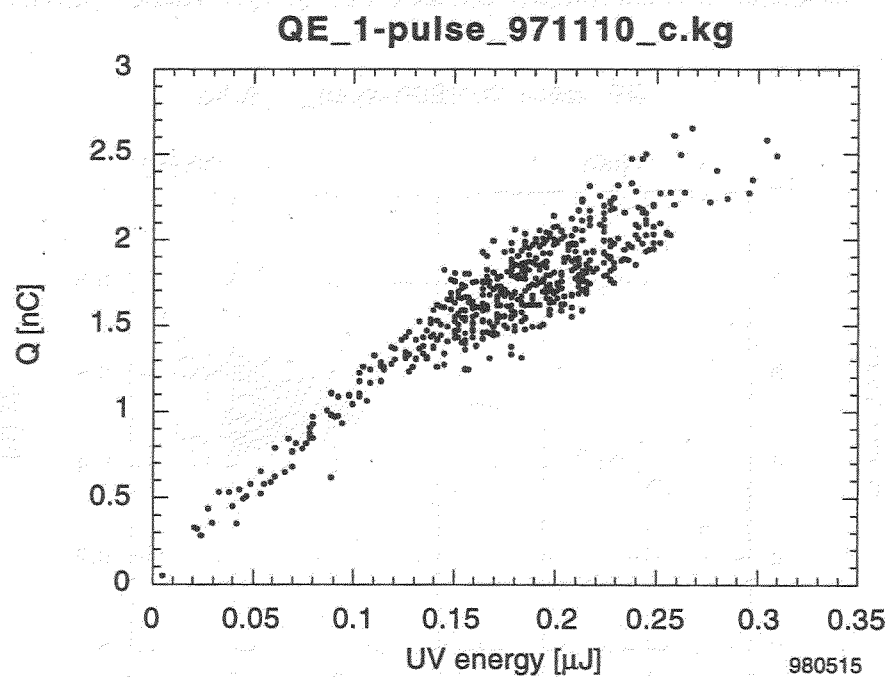

Figure 13.3. QE data with laser spot centered on photocathode. Single laser pulse photodiode calibration of UV energy.
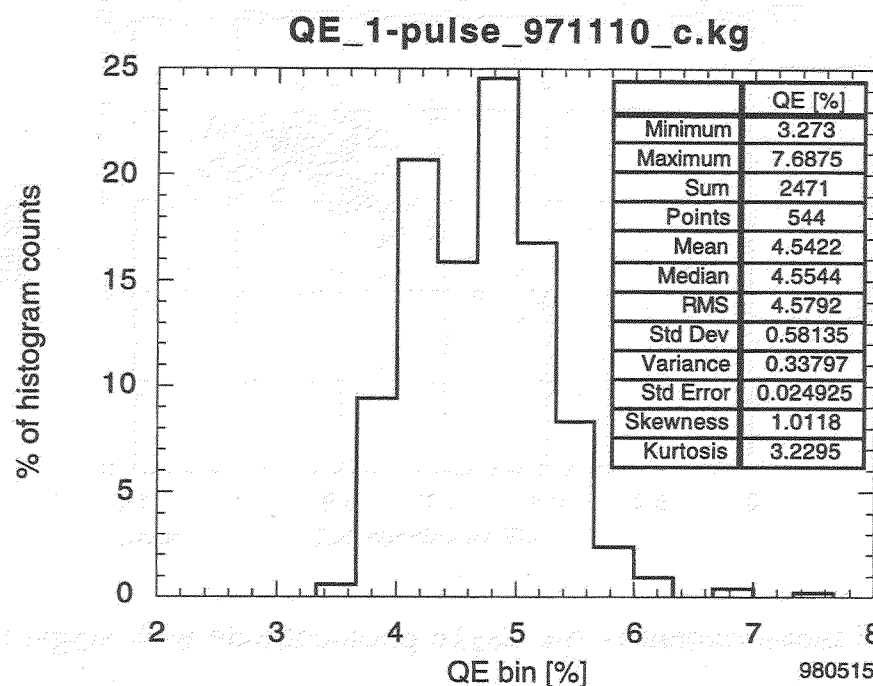
QE_1-pulse_971110_c.kg

	QE [%]
Minimum	3.273
Maximum	7.6875
Sum	2471
Points	544
Mean	4.5422
Median	4.5544
RMS	4.5792
Std Dev	0.58135
Variance	0.33797
Std Error	0.024925
Skewness	1.0118
Kurtosis	3.2295

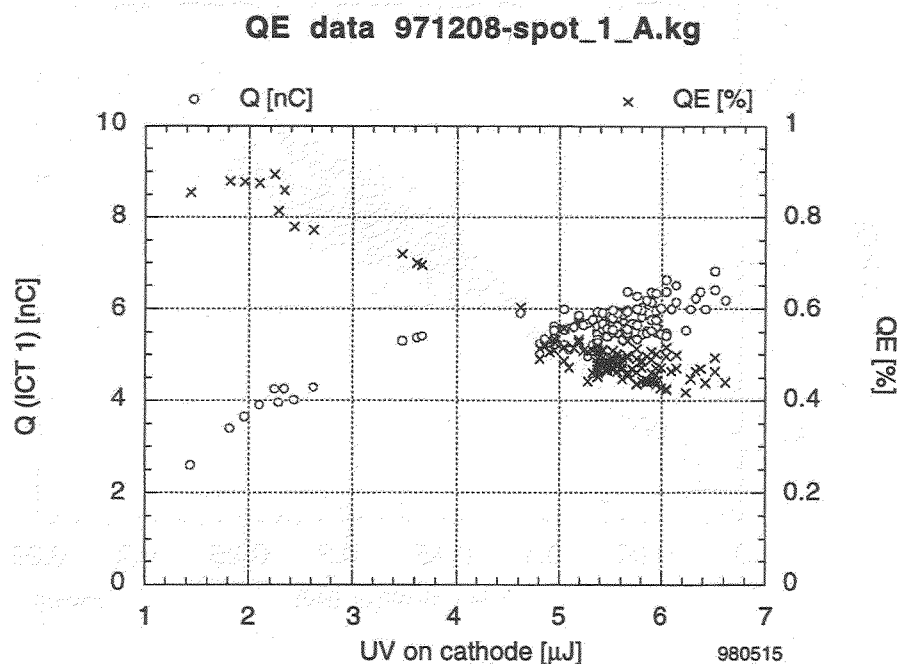**Figure 13.4.** Histogram and statistical parameters of QE values shown in Figure 13.3.

Figure 13.5. At several nC of charge, the QE decreases as a result of space charge effects.

The photo-injector and the beam line used for these experiments was disassembled in February 98. Most of the experiments we have presented will be repeated on the new beam line. These new experiments will be prepared with considerations for the lessons learned in the first set of experiments that were described in this report.

REFERENCES

[1] E. Colby, *Design, Construction, and Testing of a Radiofrequency Electron Photoinjector for the Next Generation Linear Collider*, PhD thesis, UCLA, 1997.

[2] A. Fry, *Novel Pulse Train Glass Laser for RF Photoinjectors*, PhD Thesis, UR-1492, University of Rochester, 1996.

[3] D. A. Edwards, M. J. Syphers, *An introduction to the physics of high energy accelerators*, Wiley-Interscience, New York, 1992.

[4] J.-P. Carneiro, *private communication*.

[5] K. P. Koepke, *private communication*.

[6] K. B. Unser, "Design and Preliminary Tests of a Beam Intensity Monitor for LEP," in *Proceedings of the 1989 IEEE Particle Accelerator Conference* (20-23 March 1989, Chicago, Illinois), F. Bennett & J. Kopta, Eds., IEEE Publishing, New York, 1989, p. 71-73.

[7] *Integrating Current Transformer User's Manual, Rev. 3.0*, Bergoz Precision Beam Instrumentation, Crozet, France.

[8] Julien Bergoz, *private communication*.

[9] R. E. Collin, *Foundations for Microwave Engineering*, McGraw-Hill, New York, 1966.

[10] R. H. Fowler, L. W. Nordheim, *Proceedings of the Royal Society, London*, Ser. A, **119**, p. 173 (1929).

[11] K. Halbach & R. F. Holsinger, *Particle Accelerators* **7**, p. 213 (1976).

[12] David R. Lide, Ed., *CRC Handbook of Chemistry and Physics*, 72nd Edition, CRC Press, Boca Raton, 1991, p. 12-97.

[13] H. Matsumoto, M. Akemoto, H. Hayano, T. Naito, & S. Takaba, "High Gradient Experiment by ATF," KEK Preprint 91-161, KEK, Tsukuba, Japan (November 1991).